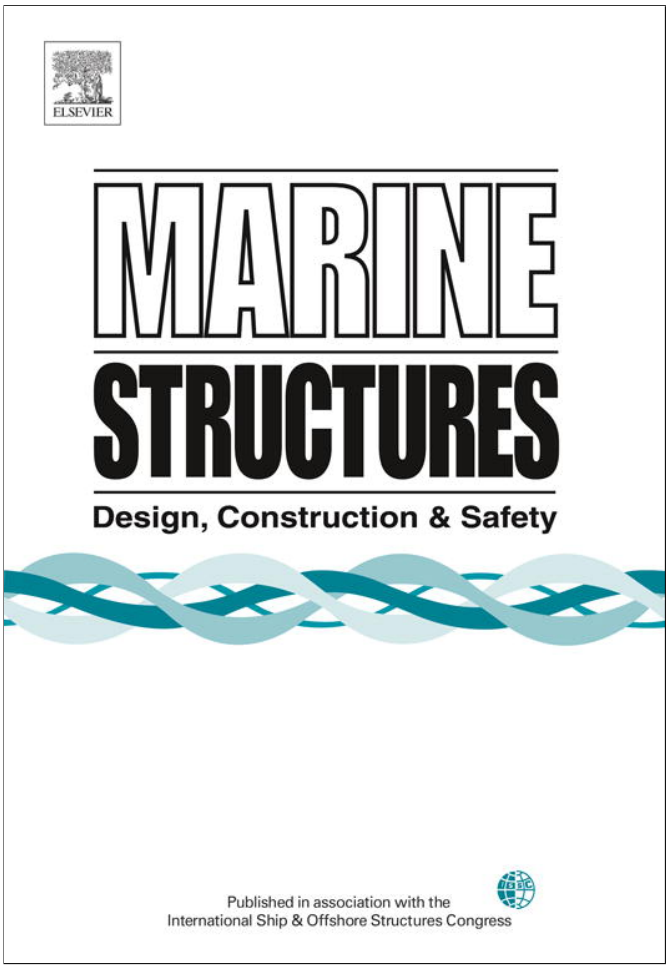

Marine Structures 38 (2014) 44–71

Contents lists available at ScienceDirect

Marine Structures

journal homepage: www.elsevier.com/locate/marstruc

Extension of the super-elements method to the analysis of a jacket impacted by a ship

Loïc Buldgen [a, *, 1], Hervé Le Sourne [b], Timothée Pire [a]

[a] University of Liège, ANAST, 1 Chemin des Chevreuils, 4000 Liège, Belgium
[b] GeM Institute, UMR 6183 CNRS, ICAM Nantes, 35 Avenue du champ de Manœuvres, 44470 Carquefou, France

ARTICLE INFO

Article history:
Received 24 February 2014
Received in revised form 12 May 2014
Accepted 16 May 2014
Available online xxx

Keywords:
Impact
Collisions on offshore wind turbines
Simplified methods
Crashworthiness
Impact on inclined cylinders

ABSTRACT

The aim of this paper is to present a simplified analytical method for estimating the crushing resistance of an oblique cylinder impacted by the stem of a striking ship. The collision angle of the vessel is arbitrary, i.e. oblique collisions are also considered in this article. The two extremities of the tube are assumed to be clamped. These developments are intended to be used for evaluating the crashworthiness of an offshore wind turbines jacket. To achieve this goal, closed-form expressions are first derived for the particular situations of a horizontal and a vertical cylinder by applying the upper-bound method. An interpolation formula is then proposed to get the resistance opposed by the tube for any inclination angle. In order to validate these theoretical developments, some comparisons are made with the results of numerical simulations. These latter are performed using the finite elements software LS-DYNA. In almost all cases, the analytical prediction of the resistance is found to be in quite good agreement with the numerical ones. Finally, another comparison is made by simulating an OSV collision with a full jacket. In this case, the theoretical model is found to be insufficient for large impact energies and points out the need of further research.

* Corresponding author. University of Liège, Faculty of Applied Sciences, ANAST, 1 Chemin des Chevreuils, 4000 Liège, Belgium. Tel.: +32 (0) 4 366 48 59, +32 (0) 478 50 21 88 (mobile); fax: +32 (0) 4 366 91 33.
E-mail addresses: L.Buldgen@ulg.ac.be (L. Buldgen), herve.lesourne@icam.fr (H. Le Sourne), tpire@student.ulg.ac.be (T. Pire).
[1] PhD Student supported by the FRIA (Belgian National Fund for Scientific Research).

http://dx.doi.org/10.1016/j.marstruc.2014.05.002
0951-8339/

1. Introduction

Nowadays, it is more and more important for the humanity to produce energy in a sustainable manner. This is particularly true for electricity generation, which may no longer be provided by classical nuclear or coal power plants, which are considered to be too dangerous for the environment. Amongst all the existing ways of producing electricity, offshore wind turbines appear to be a promising one and many governments are supporting their development all over the world.

Amongst all the loads to be considered when dimensioning an offshore wind turbine supporting system, the case of a ship collision has to be treated carefully as it may have very severe consequences for the structure and the vessel. This is precisely the subject of this paper, in which an impact occurring between a given ship and the jacket of a non-floating offshore wind turbine (Fig. 1) is considered.

To assess the impact resistance of the jacket, it is of course possible to resort to finite elements simulations, as this has been done by Amdahl and Holmas [1], Vredeveldt and Schipperen [2], Biehl [3] or Amdahl and Johansen [4] for example. As both the ship and the collided structure have to be finely meshed, the modeling effort can be important. Such approaches are also time-expensive and consequently not convenient at the beginning of the design process, when the final properties of the structure are not completely fixed. Moreover, in the framework of a full collision risk analysis where different striking vessels and collision scenarios have to be considered, a simplified analytical approach allowing for a rapid approximation of the jacket crashworthiness becomes more relevant.

A basic idea consists in idealizing the jacket as a set of individual tubes (Fig. 1) with particular connections at their extremities. In this paper, it is assumed that the deformations only take place on the cylinders in contact with the bow, all the adjacent being unaffected. This hypothesis is the single restriction postulated in this paper.

The problem of an impact occurring on a cylinder has already been treated in the literature by Hoo Fatt and Wierzbicki [5], Wierzbicki and Suh [6] or Zeinoddini, Harding and Parke [7], amongst others. All these authors have considered the case of a concentrated load acting at the mid-length of a cylinder having a length L and a radius R (Fig. 2(a)). Nevertheless, this work is insufficient, as the analysis of a jacket component impacted by a ship (Fig. 2(b)) is similar to the one of an eccentric oblique impact, initially located at a distance L_1 from the left support, occurring on a cylinder having an inclination ζ and where the striking direction is characterized by an angle α. Moreover, the bow shape may also have an influence on the deformation pattern, which is not necessarily the same as for a concentrated force. The work detailed in this paper goes one step further by accounting for all these particularities and aims to be a generalization of what has already been done by many authors.

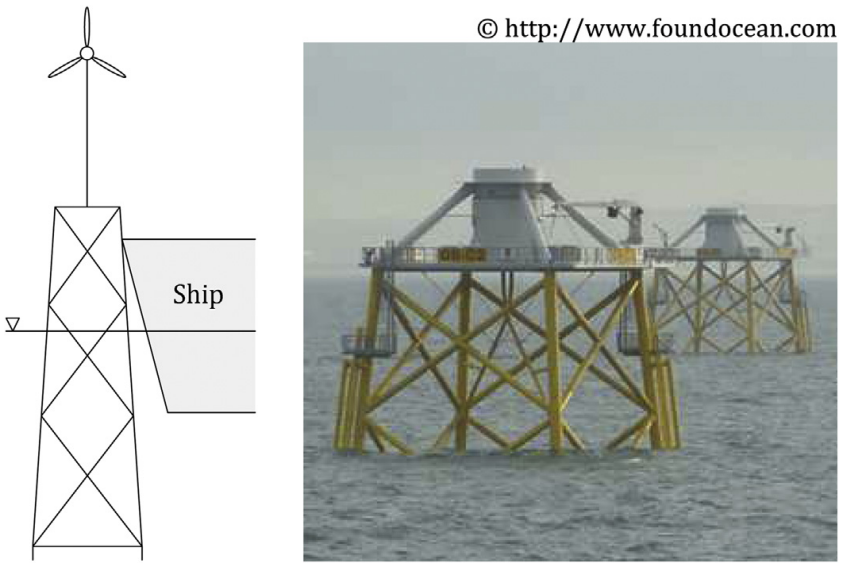

Fig. 1. Collision on an offshore wind turbine.

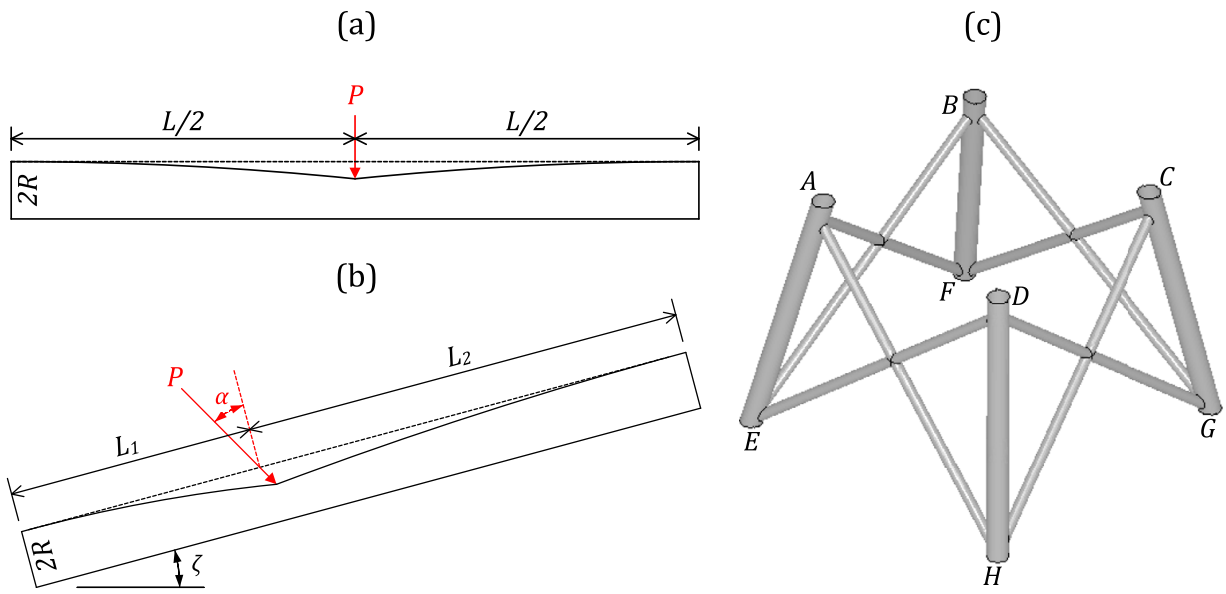

Fig. 2. Description of the collision configuration.

2. Description of the collision scenario

When a ship collides the jacket of an offshore wind turbine, the direction followed by the vessel and the inclination of the struck cylinder are arbitrary. The collision scenario is therefore defined by the relative position between the ship and the impacted tube.

Let us first consider the portion of the jacket depicted on Fig. 2(c) and suppose that the cylinder *CH* is collided by the stem. By denoting *C′* the vertical projection of point *C* over the horizontal plane *EFGH* (Fig. 3(a)), the vertical plane *CHC′* (Fig. 3(a) and (b)) containing *CH* is used for locating the vessel with respect to the struck tube. A new reference frame (*X*,*Y*,*Z*) is defined to characterize the position the vessel, having its origin in *C* and oriented so that the horizontal *X* axis is normal to *CHC′* and *Z* is vertical.

Regarding the ship stem, the shape of its uppermost deck is idealized by a parabola described by its two radii (*p*,*q*) and its center *S* (Fig. 4), which is also taken as the origin of the local coordinate frame

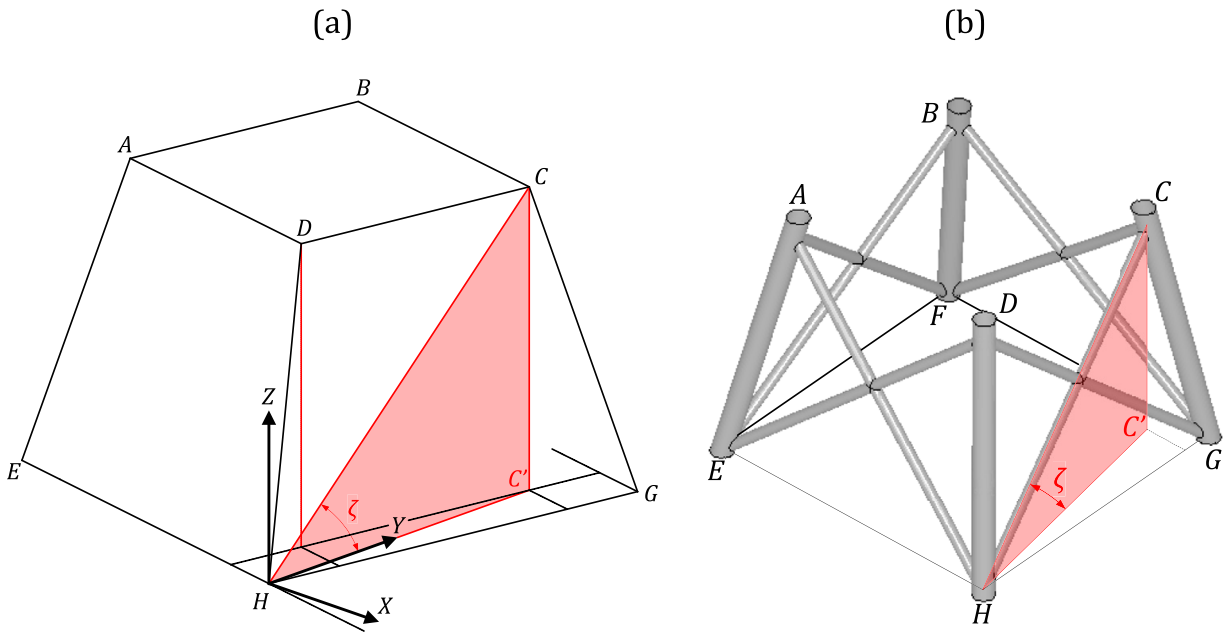

Fig. 3. Three dimensional view of the vertical plan containing the impacted cylinder.

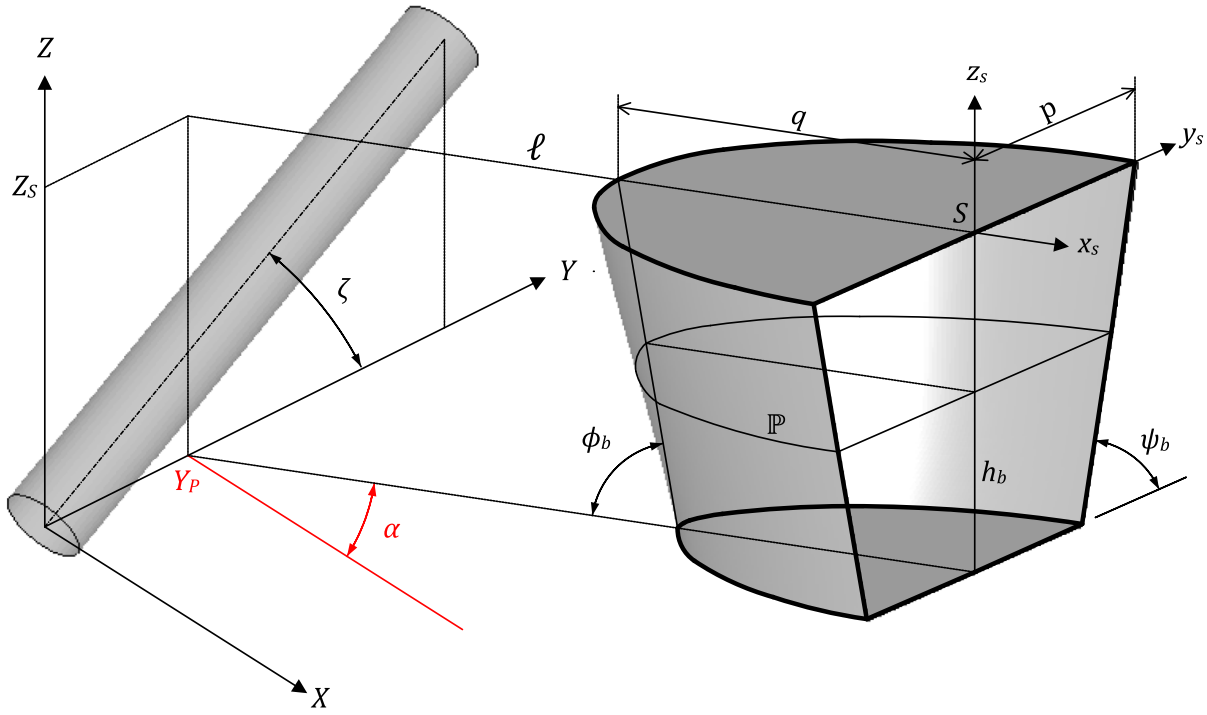

Fig. 4. Relative position of the striking vessel with respect to the cylinder.

(x_s,y_s,z_s). The stem and side angles are respectively denoted ϕ_b and ψ_b, while the total distance separating the uppermost and lowermost decks is designated by h_b. Using these notations, the equation of the curve $\mathbb{P}$ corresponding to the intersection between the ship bow and a horizontal plane located at z_s (Fig. 4) has the following equation:

$$\mathbb{P}\equiv\frac{x_s^2}{(q-z_s\cot\phi_b)^2}+\frac{y_s^2}{(p-z_s\cot\psi_b)^2}=1\ ;\quad -h_b\le z_s\le 0 \tag{1}$$

It is now possible to further define the trajectory of the stem in the reference frame (X,Y,Z) by following the point S. In fact, the vessel is supposed to move along an oblique straight line ℓ (Fig. 4), making an angle α with the horizontal X axis and crossing the plane (Y,Z) located at Y_P. The parameters Y_P and α are sufficient to locate the point S along X and Y axes, but its position along vertical Z axis is still unknown. This latter will be simply denoted by Z_S, so that the three parameters (α,Y_P,Z_S) are the data required to completely define the relative position of the bow with respect to the tube.

The cylinder geometry is finally described by its radius R, its thickness t_p, its length L and its inclination angle ζ with respect to the horizontal plane (X,Y), as depicted on Figs. 3 and 4.

3. Impact on a vertical cylinder

3.1. Deformation mechanism

As a first step, let us start by analyzing the particular case of an impact on a vertical cylinder, i.e. for which $\zeta=\pi/2$. The collision configuration of Fig. 5 shows that the cylinder is first impacted by the uppermost deck. The impact kinematics is therefore analyzed in the horizontal plane located at $Z=Z_S$ (or $z_s=0$). Fig. 6 presents a top view of the relative position occupied by the vessel and the cylinder when the first contact appears. For clarity, the dimensions of the tube have been intentionally exaggerated with respect to those of the ship.

For convenience, a new reference frame (x,y,z) located at the center of the cylinder and parallel to (x_s,y_s,z_s) is introduced. If we denote by (x_S,y_S) the coordinates of point S with respect to (x,y,z), then the

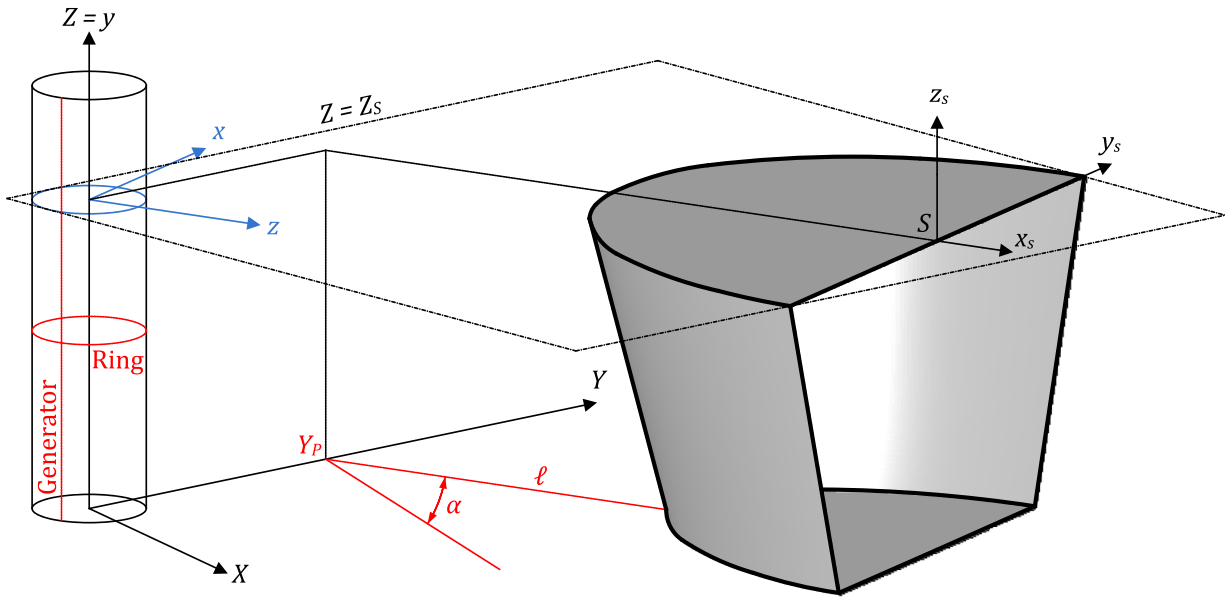

Fig. 5. Collision configuration for an impact on a vertical cylinder.

equations of curves $\mathbb{P}$ and $\mathbb{C}$ respectively describing the stem and the cylinder in the horizontal plane $z_s = 0$ may be obtained from (1):

$$\mathbb{P}\equiv\frac{(x-x_S)^2}{p^2}+\frac{(z-z_S)^2}{q^2}=1 \quad \mathbb{C}\equiv\frac{x^2}{R^2}+\frac{z^2}{R^2}=1 \tag{2}$$

By expressing that $\mathbb{C}$ and $\mathbb{P}$ are initially tangent (Fig. 6), the coordinates (x_I,z_I) of the first contact point I can be calculated and equation (2) gives the initial position (x_S,z_S) of point S.

When the ship is moving forwards, for a given value of the penetration δ, the section of the cylinder is crushed by an amount $a(\delta) = \overline{AI} \leq \delta$. From Fig. 6, the crushing distance $a(\delta)$ is found by calculating the intersection A between the current position of the stem $\mathbb{P}(\delta)$ and the straight line OI relating the origin O to the initial contact point I. The equation of $\mathbb{P}(\delta)$ may be directly derived from (2):

$$\mathbb{P}(\delta)\equiv z=-\frac{q}{p}\sqrt{p^2-(x-x_S)^2}+z_S-\delta \quad OI\equiv z=x\cot\beta \tag{3}$$

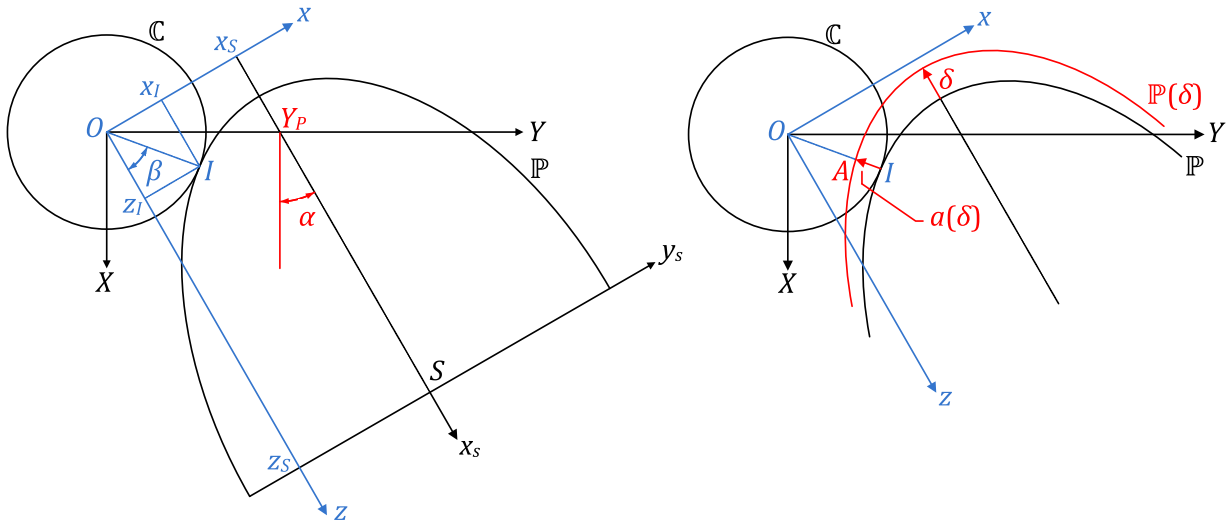

Fig. 6. Collision configuration in the horizontal plane $Z = Z_S$.

The coordinates (x_A,z_A) of point A are the particular values for which the two equations mentioned in (3) are simultaneously satisfied and it can be shown so x_A is given by:

$$x_A = \frac{q^2 x_S - p^2(\delta - z_S)\cot\beta - pq\,\mathrm{sign}(x_S)\sqrt{q^2 + p^2\cot^2\beta - (x_S\cot\beta + \delta - z_S)^2}}{q^2 + p^2\cot^2\beta} \tag{4}$$

which may be used to calculate $a(\delta) = |(x_I - x_A)/\sin\beta|$. As soon as the crushing distance is known, the next step consists in imagining a realistic deformation pattern for the cylinder cross-section. To do so, let us consider the straight line d that is tangent to $\mathbb{P}$ (Fig. 7a). When $\delta = 0$, d is going through the initial contact point I and is tangent to both $\mathbb{C}$ and $\mathbb{P}$. However, as the ship is moving forwards ($a(\delta) > 0$), d remains tangent to $\mathbb{P}(\delta)$ and goes through the intersection point A (Fig. 7(a)). The angle made by d and the horizontal x axis, denoted by γ, is used for defining the deformation pattern of the tube cross-section. Moreover, as detailed hereafter, considering the tangent line d and the inclination angle γ is an approximate manner of accounting for the shape of striking stem. The expression of γ is found by considering the equation of $\mathbb{P}(\delta)$ given by (3), i.e.:

$$\tan\gamma = \left[\frac{\partial z}{\partial x}\right]_{x=x_A} \Leftrightarrow \gamma = \mathrm{atan}\left(\frac{\mathrm{q}}{\mathrm{p}}\frac{\mathrm{x_S} - \mathrm{x_A}}{\sqrt{\mathrm{p}^2 - (\mathrm{x_A} - \mathrm{x_S})^2}}\right) \tag{5}$$

where x_A is given by (4) and x_S by the initial position of the ship at the beginning of the impact. The assumed deformation pattern related to γ is depicted on Fig. 7(a), where the cylinder section is shown to be crushed over a distance $a(\delta) = \overline{AI}$. The deformation pattern associated with $a(\delta)$ is then defined with help of the tangent line $d \equiv BC$ and the inclination angle γ introduced here above.

Let us start by considering the straight line ED perpendicular to BC and such that $\overline{BD} = \overline{CD}$. In fact, ED is the bisection of BC and E is located at the intersection of the initial cylinder cross-section $\mathbb{C}$ (Fig. 7(b)). By imposing symmetry condition with respect to ED, we can simply analyze the upper half $EFBD$ of the deforming cross-section, which may be split into three different portions:

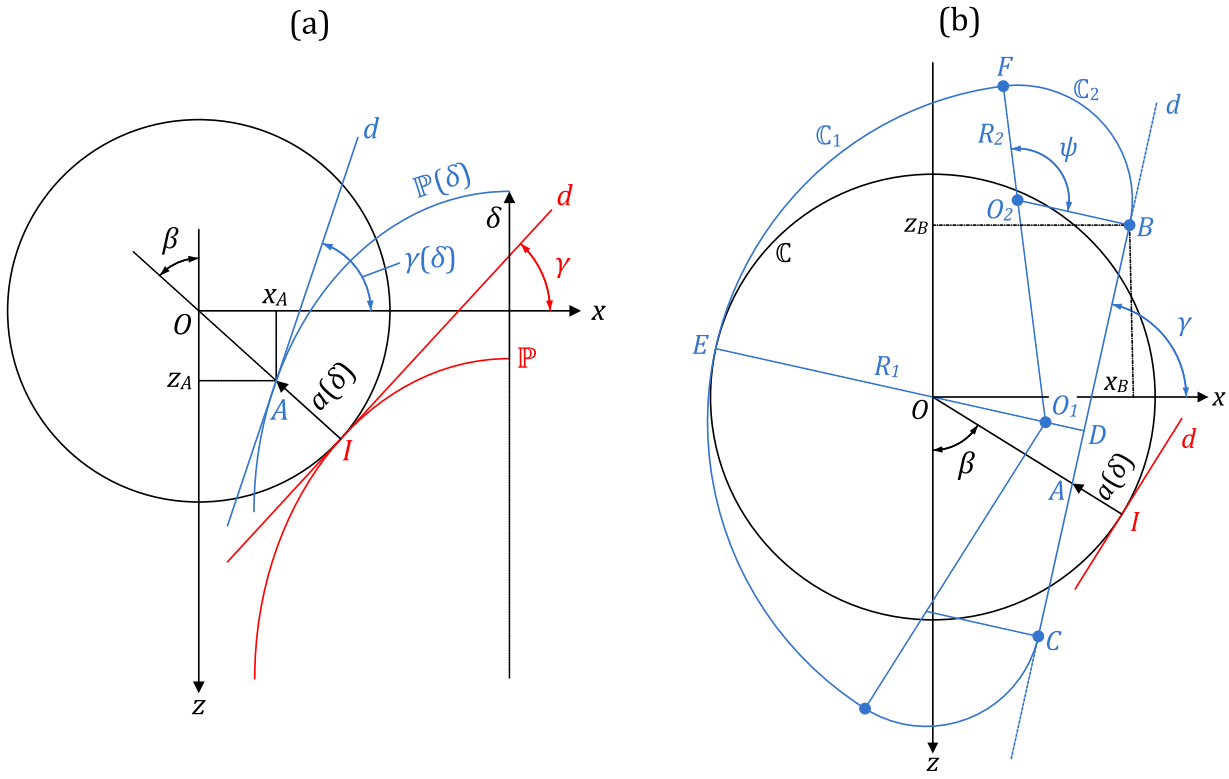

Fig. 7. Deformation pattern of the cylinder cross-section.

- The circular arc $\mathbb{C}_1 \equiv EF$, characterized by its radius R_1 and its center O_1. For a given value of δ, the current opening of $\mathbb{C}_1$ is equal to $\pi - \psi$.
- The circular $\mathbb{C}_2 \equiv BF$, characterized by its radius R_2 and its center O_2. For a given value of δ, the current opening of $\mathbb{C}_1$ is equal to ψ.
- The straight segment BD having the same inclination γ than the tangent line d and characterized by a total length equal to $(R_1 - R_2)\sin\psi$.

Considering such a deformation pattern requires the calculation of R_1, R_2 and ψ for defining correctly the deformed cross-section. To do so, we can start by deriving the coordinates (x_B,z_B) of point B. From Fig. 7(b), it can be shown that:

$$\begin{aligned} x_B &= (R_1 - R)\cos\gamma + (R_1 - R_2)\cos(\gamma + \psi) \\ z_B &= (R_1 + R_2 - R)\cos\gamma + (R_1 - R_2) + (R_1 - R_2)\cos(\gamma + \psi) \end{aligned} \tag{6}$$

On the other hand, as d has an inclination γ and is going through the point A, its equation may be written as follow:

$$d \equiv z = x_A \cot\beta - (x - x_A)\tan\gamma \tag{7}$$

where x_A and γ are respectively given by equations (4) and (5). The angle β is defined on Figs. 6 and 7(b) with help of the initial contact point I. As $B \in d$, the coordinates (x_B,z_B) given in (6) have to satisfy (7), which allows us to find a first relation between R_1, R_2 and ψ:

$$R_2 = \frac{R + x_A(\cot\beta\cos\gamma + \sin\gamma) - R_1(1 + \cos\psi)}{1 - \cos\psi} \tag{8}$$

An additional relation may be found by assuming, as done in references [6,7], that the initial perimeter of $\mathbb{C}$ remains unchanged during the crushing process. This may be mathematically translated by the following relation:

$$R_1(\pi - \psi) + R_2\psi + \overline{BD} = \pi R \Leftrightarrow \mathrm{R}_1(\pi - \psi) + \mathrm{R}_2\psi + (\mathrm{R}_1 - \mathrm{R}_2)\sin\psi = \pi\mathrm{R} \tag{9}$$

Substituting (8) in (9) leads to an explicit expression for R_1 as a function ψ. It may be shown that:

$$R_1 = \frac{\pi R(1 - \cos\psi) - (\psi - \sin\psi)(R + x_A(\cot\beta\cos\gamma + \sin\gamma))}{\pi(1 - \cos\psi) - 2(\psi - \sin\psi)} \tag{10}$$

From Fig. 7(b), it appears that $\psi = \pi$ when the section is completely crushed. If we denote by ψ_0 the initial value of ψ when $\delta = 0$, we may adopt the subsequent linear variation of ψ with the penetration δ:

$$\psi = \psi_0 + (\pi - \psi_0)\frac{\delta}{\delta_f} \tag{11}$$

where δ_f is the final value of δ for which the section is completely crushed. The value of ψ_0 is still unknown but will be fixed later on. The deforming pattern depicted on Fig. 7(b) is entirely characterized with help of equations (8), (10) and (11) and the next step consists in deriving the displacement field associated to this mechanism.

3.2. Definition of the displacement field

The goal of this section is to define the displacement field associated with the deformation pattern depicted on Fig. 7(b) and reproduced on Fig. 8(a), where ED is still a line of symmetry and H is the intersection between ED and $\mathbb{C}$. Let us now consider any point M belonging to $\mathbb{C}$ and having the coordinates $(x_M,z_M) = (R\cos\theta,R\sin\theta)$. In the deformed configuration $\mathbb{C}'$ depicted on Fig. 8(a), M is moved to

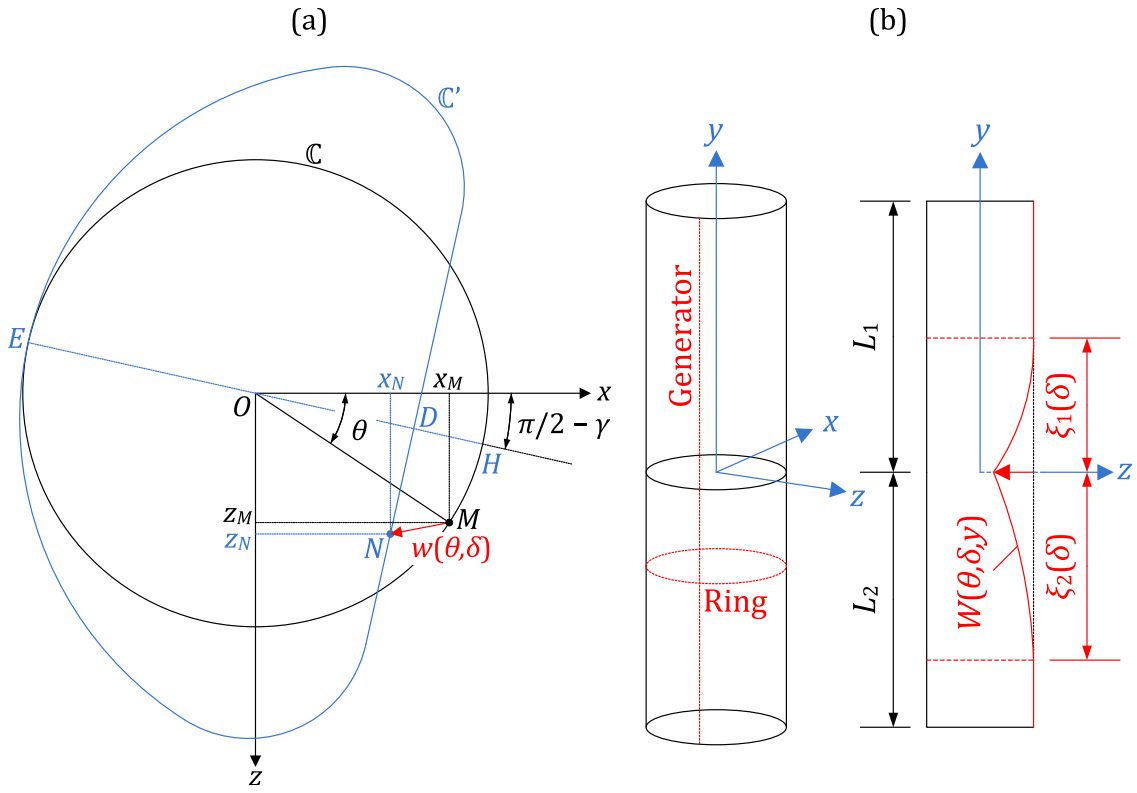

Fig. 8. Definition of the displacement field.

another point N located in (x_N,z_N). The perimeter of the cross-section remaining constant, the length of HM measured along $\mathbb{C}$ is equal to the length of DN in the deformed configuration $\mathbb{C}'$, which writes:

$$\overline{DN} = R(\theta + \gamma - \pi/2) \tag{12}$$

where $\overline{DN}$ is the curvilinear length between D and N measured along $\mathbb{C}'$. By developing the previous equation, it is possible to find (x_N,z_N) and to calculate the displacement $w(\theta,\delta)$ of point M, i.e. the distance $\overline{MN}$ (Fig. 8(a)):

$$w(\theta,\delta) = \sqrt{(x_N - x_M)^2 + (z_N - z_M)^2} \tag{13}$$

As the mathematical derivation of $w(\theta,\delta)$ is particularly fastidious, we won't give any detail about it in this paper, but additional information may be found in references [6,9,10]. By taking the time derivative of (13), we get the velocity field $\dot{w}(\theta,\delta)$.

So far, only the displacements taking place in the horizontal plane $Z = Z_S$ (Fig. 5) have been considered. Nevertheless, it is clear that the entire cylinder is deforming during the impact, so we need to extrapolate the velocity $\dot{w}(\theta,\delta)$ along the vertical y axis.

This can be achieved by proceeding in a similar way than Wierzbicki and Suh [6], who considered that the deforming portion of the tube is progressively growing with the indentation δ. Consequently, looking at the deformation in the plane $x = 0$ (Fig. 8(b)), we can imagine that the cylinder is linearly indented over the portion $-\xi_2 \le y \le \xi_1$, while the other parts $-L_2 \le y < \xi_2$ and $\xi_1 < y \le L_1$ are assumed to remain undamaged:

$$\begin{aligned}
\dot{W}(\theta,\delta,y) &= \dot{w}(\theta,\delta)\left(1 - \frac{y}{\xi_1(\delta)}\right) \quad \text{if} \quad y \in [0;\xi_1(\delta)] \\
\dot{W}(\theta,\delta,y) &= \dot{w}(\theta,\delta)\left(1 + \frac{y}{\xi_2(\delta)}\right) \quad \text{if} \quad y \in [-\xi_2(\delta);0] \\
\dot{W}(\theta,\delta,y) &= 0 \quad \text{if} \quad y \in [L_2;-\xi_2(\delta)[\cup]\xi_1(\delta);L_1]
\end{aligned} \tag{14}$$

where $\xi_1 \le L_1$ and $\xi_2 \le L_2$ will be fixed later on.

3.3. Local crushing resistance

To derive analytically the crushing resistance, the basic idea is to apply the upper bound theorem (see Jones [8] for more details), by supposing that the cylinder is made of a rigid-plastic material characterized by a flow stress σ_0.

As a first step, similarly to Wierzbicki and Suh [6], we suppose that the impacted cylinder is composed of generators supported by independent rings that are free to slide on each other without shearing (see Figs. 5 and 8(b)). As a consequence, the total energy rate $\dot{E}$ of to the crushing mechanism is simply given by:

$$\dot{E} = \dot{E}_r + \dot{E}_g \tag{15}$$

where $\dot{E}_r$ and $\dot{E}_g$ are the energy rates of the rings and the generators.

3.3.1. Energy rate of the rings

Let us start by considering the energy rate $\dot{E}_b$ related to the deformation of the central section depicted on Fig. 7(b). The expression of $\dot{E}_b$ can be derived by following a very similar procedure than the one exposed in references [6,7]. As justified by Wierzbicki in Ref. [6], $\dot{E}_b$ is mainly due to bending effects taking place over the cross-section. Fig. 7(b) shows that the curvatures χ_1 and χ_2 characterizing the circular arcs $\mathbb{C}_1$ and $\mathbb{C}_2$ are not the same, as we have $\chi_1 = 1/R_1$ and $\chi_2 = 1/R_2$. The curvature is therefore discontinuous at the junctions $\mathbb{C}_1 \cap \mathbb{C}_2$ and $\mathbb{C}_2 \cap BD$, which implies moving plastic hinges to be located at points B and F. Consequently, the energy dissipation is due to both the modification of the curvature along $\mathbb{C}_1$ and $\mathbb{C}_2$, and the bending effects occurring inside the moving plastic hinges, so we have:

$$\dot{E}_b = 2m_0 \left(\frac{V_B}{R_2} + \left(\frac{1}{R_2} - \frac{1}{R_1} \right) V_F + \int_F^E \dot{\chi}_1 \mathrm{d}l + \int_D^F \dot{\chi}_2 \mathrm{d}l \right) \tag{16}$$

where $m_0 = \sigma_0 t_p^2/4$ is the cylinder bending capacity per unit of length. The first and second terms of (16) correspond to the energy dissipated inside the hinges B and F. These latter are characterized by the velocities V_B and V_F and it can be demonstrated from Fig. 7(b) that:

$$\begin{aligned} V_B &= (R_1 - R_2)\dot{\psi} - (\pi - \psi)\dot{R}_1 - \psi \dot{R}_2 = \left((R_1 - R_2)\frac{\partial \psi}{\partial \delta} - (\pi - \psi)\frac{\partial R_1}{\partial \delta} - \psi \frac{\partial R_2}{\partial \delta} \right) \dot{\delta} \\ V_F &= R_1 \dot{\psi} - (\pi - \psi)\dot{R}_1 = \left(R_1 \frac{\partial \psi}{\partial \delta} - (\pi - \psi)\frac{\partial R_1}{\partial \delta} \right) \dot{\delta} \end{aligned} \tag{17}$$

Similarly, the third and fourth terms of (16) describe the change of curvature occurring in $\mathbb{C}_1$ and $\mathbb{C}_2$ respectively. As $\chi_1 = 1/R_1$ and $\chi_2 = 1/R_2$, these curvilinear integrals are quite easy to evaluate and may be written as:

$$\int_F^E \dot{\chi}_1 \mathrm{d}l = \frac{\pi - \psi}{R_1} \frac{\partial R_1}{\partial \delta} \dot{\delta} \;\; ; \;\; \int_D^F \dot{\chi}_2 \mathrm{d}l = \frac{\psi}{R_2} \frac{\partial R_2}{\partial \delta} \dot{\delta} \tag{18}$$

By introducing (17) and (18) in (16), a closed-form expression of $\dot{E}_b$ is derived, where $\partial R_1/\partial \delta$, $\partial R_2/\partial \delta$ and $\partial \psi/\partial \delta$ are obtained by derivation of equations (10), (8) and (11) respectively.

The theoretical developments performed here above are only valid for the central cross-section located in the horizontal plane $y = 0$ (Fig. 5), but a similar procedure should be followed for all the rings located along the vertical y axis. Nevertheless, if we want to analyze the situation for $y \neq 0$, it is clear that the deformation pattern of Fig. 7(b) is not valid anymore because the crushing distance is not equal to $a(\delta)$ in this case. In fact, if $y \neq 0$, the penetration has to be found by integrating the velocity field postulated in (14) with the particular initial condition $W(\theta,\delta,y) = 0$ for $\delta = 0$. Unfortunately, it is

impossible to apply such an approach if we want to obtain a closed-form solution. As suggested in Ref. [6], an approximate solution is derived by calculating the bending dissipation in a section located at $y \neq 0$ through a linear interpolation of $\dot{E}_b$. The total energy rate $\dot{E}_r$ of the rings located along the vertical y axis is then given by:

$$\dot{E}_r = \int_{-\xi_2}^{0} \dot{E}_b \left(1 + \frac{y}{\xi_2}\right) \mathrm{d}y + \int_{0}^{\xi_1} \dot{E}_b \left(1 - \frac{y}{\xi_1}\right) \mathrm{d}y = \dot{E}_b \frac{\xi_1 + \xi_2}{2} \tag{19}$$

where $\dot{E}_b$ is obtained by using equation (16).

3.3.2. Energy rate of the generators

As mentioned here above, the displacement field $W(\theta,\delta,y)$ acting on a generator may be found by integrating the velocity profile. Equation (14) shows that both the length and the curvature of the generator change when $W(\theta,\delta,y)$ increases, which implies membrane and bending effects that are difficult to evaluate analytically. A conservative hypothesis is then to neglect the flexural energy, which means that the dissipation is entirely coming from the membrane strains developing inside the generator. As each generator is supposed to slide freely on the rings without shearing, the only contribution to the membrane energy rate comes from an axial elongation. The corresponding deformation rate $\dot{\varepsilon}_m$ is given by:

$$\dot{\varepsilon}_m(\theta, \delta, y) = \frac{\partial W}{\partial y} \frac{\partial \dot{W}}{\partial y} \tag{20}$$

Consequently, the total membrane energy rate $\dot{E}_m$ associated to a particular generator located at the angular position θ is calculated by integrating $\dot{\varepsilon}_m$ along the deforming part of the cylinder:

$$\dot{E}_m(\theta, \delta) = n_0 \int_{-\xi_2}^{\xi_1} \dot{\varepsilon}_m(\theta, \delta, y) \mathrm{d}y = n_0 \dot{\delta} \left(\frac{1}{\xi_1} + \frac{1}{\xi_2}\right) w(\theta, \delta) \frac{\partial w}{\partial \delta} \tag{21}$$

where $n_0 = \sigma_0 t_p$ is the axial resistance of the cylinder per unit of length. Here, $w(\theta,\delta)$ is the displacement field of the central cross-section given by (13) and $\partial w/\partial\delta$ is the corresponding velocity. It is worth noting that $\dot{E}_m$ corresponds to a single generator located at a certain angular position θ. So calculating $\dot{E}_g$ requires to account for all the generators, i.e.:

$$\dot{E}_g = \int_{\mathbb{C}} \dot{E}_m(\theta, \delta) \mathrm{d}l = 2Rn_0 \dot{\delta} \left(\frac{1}{\xi_1} + \frac{1}{\xi_2}\right) \int_{0}^{2\pi} w(\theta, \delta) \frac{\partial w}{\partial \delta} \mathrm{d}\theta = \left(\frac{1}{\xi_1} + \frac{1}{\xi_2}\right) \dot{E}'_m \tag{22}$$

Since it is practically impossible to find a closed-form for $\dot{E}'_m$, equation (22) is solved by numerical integration.

3.3.3. Virtual work principle

Once all the contributions have been calculated, equations (15), (19) and (22) are used to find the total energy rate:

$$\dot{E} = \dot{E}_b \frac{\xi_1 + \xi_2}{2} + \left(\frac{1}{\xi_1} + \frac{1}{\xi_2}\right) \dot{E}'_m \tag{23}$$

According to the virtual velocity principle (see reference [8] for more details), the internal energy rate is equated to the external power developed by the crushing resistance $P_l(\delta)$ of the vertical cylinder.

As depicted on Fig. 7(a), for a given penetration δ, the displacement of the contact point I is equal to $a(\delta)$. Consequently, applying the virtual work principle leads to:

$$P_l(\delta)\dot{a}(\delta) = \dot{E}_b\frac{\xi_1+\xi_2}{2} + \left(\frac{1}{\xi_1}+\frac{1}{\xi_2}\right)\dot{E}'_m \Leftrightarrow \mathrm{P_l}(\delta) = \left(\mathrm{E_b}\frac{\xi_1+\xi_2}{2} + \left(\frac{1}{\xi_1}+\frac{1}{\xi_2}\right)\mathrm{E'_m}\right)\left(\frac{\partial \mathrm{a}}{\partial \delta}\right)^{-1} \tag{24}$$

where $E_b = \dot{E}_b/\delta$ and $E'_m = \dot{E}'_m/\delta$. The last step is then to evaluate ξ_1 and ξ_2. This can be achieved by minimizing (24):

$$\frac{\partial P_l}{\partial \xi_1} = 0 \;\; ; \quad \frac{\partial P_l}{\partial \xi_2} \Leftrightarrow \xi_1(\delta) = \min\left(\sqrt{2\mathrm{E'_m}/\mathrm{E_b}}; \mathrm{L_1}\right) \quad ; \xi_2(\delta) = \min\left(\sqrt{2\mathrm{E'_m}/\mathrm{E_b}}; \mathrm{L_2}\right) \tag{25}$$

As a final remark, it is worth bearing in mind that there is still one undefined parameter. Indeed, if we go back to equation (11), we see that the initial value ψ_0 of the angle ψ remains unknown. By comparisons with numerical simulations (see Section 5.2), this one is fixed to $3\pi/4$. This value is quite close to the one recommended in Refs. [6,7,10].

3.4. Global crushing resistance

All the theoretical developments presented in Sections 3.1–3.3 with the objective of modeling a localized indentation of the tube. In other words, this means that the cylinder is supposed to be crushed without exhibiting any beam-like behavior. In this case, we say that the resistance $P_l(\delta)$ is said to be provided through a *local* deforming mode. However, droptests on cylinders show that for a given penetration, the tube is forced into an overall bending motion. The deformations are not any longer confined in a localized area near the impact point but are affect the entire structure. In that case, we say that the resistance $P_g(\delta)$ is said to be provided through a *global* deforming mode.

Finite elements simulations of full-scale ship-jacket collisions show that at the beginning of the impact, the crushing resistance of a leg or a brace is essentially coming from the local mode [11]. But as the ship is moving forwards, the global mode is progressively activated. Consequently, there is a switch in the behavior of the tube. In reality, this transition is quite smooth but in our mathematical model. The activation of the global deforming mode is supposed to occur abruptly, for a particular value δ_t of the penetration. As depicted on Fig. 9(a), the final resistance $P_v(\delta)$ is evaluated as follow:

$$P_v(\delta) = P_l(\delta) \quad \text{if} \quad \delta \leq \delta_t \;\; ; \quad P_v(\delta) = P_g(\delta) \quad \text{if} \quad \delta > \delta_t \tag{26}$$

The final step to get $P_v(\delta)$ is then to evaluate $P_g(\delta)$. In fact, the global behavior of the tube may be studied with the classical theory of beams. If the extremities of the cylinder are totally restrained, then the global resistance $P_g(\delta)$ is derived under the assumption of a three plastic hinges mechanism. This one is represented on Fig. 9(b), where M_0 is the fully plastic bending moment of the initial circular cross-section $\mathbb{C}$. If the thickness t_p being small in comparison with the radius R, we have $M_0 = 4R^2\sigma_0 t_p$. At the beginning of the global mode, M_0 has to be reached at the two extremities of the tube, as the corresponding sections are supposed to be undamaged. However, this is not the case for the central cross-section, where only a reduced value $\xi(\delta)M_0 \leq M_0$ can be reached because of the crushing of the cross-section. In fact, $\xi(\delta)M_0$ is the plastic bending moment calculated by considering the deformed cross-section depicted on Fig. 7(b) for a given value of δ. So the main issue is now to evaluate the reduction factor $\xi(\delta)$, which is a quite arduous task.

Considering the deformed cylinder section depicted on Fig. 7(b), it is difficult to evaluate precisely the reduction factor $\xi(\delta)$. As suggested by De Oliveira [10], $\xi(\delta)$ may be derived for an approximate cross-section, obtained by neglecting $\mathbb{C}_2$ and extending $\mathbb{C}_1$ till the tangent line d. Doing so, we get the semi-circular section depicted on Fig. 9(c) for which it is much easier to evaluate the plastic bending

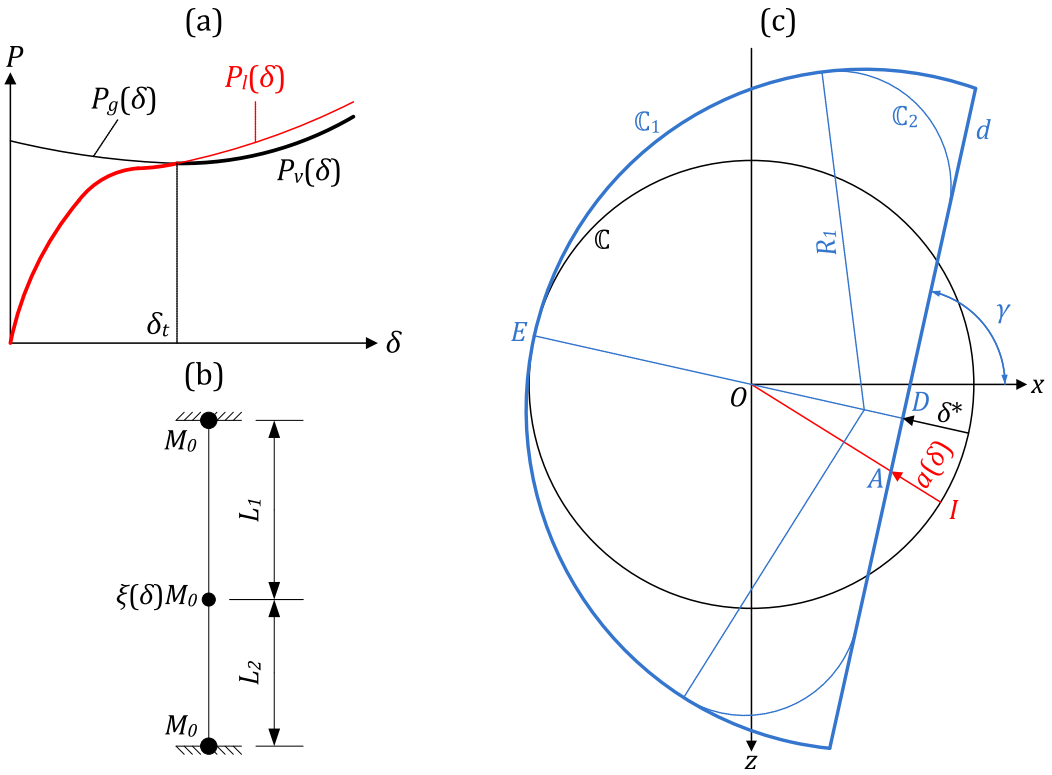

Fig. 9. (a) Evaluation of the total resistance; (b) Activation of the global plastic mechanism for a given penetration δ; (c) Reduced cross-section.

moment. For the sake of conciseness, the detailed derivation of $\xi(\delta)$ will not be reported here. We finally get:

$$\xi(\delta) = \frac{1}{2}\left(\left(\frac{\delta^*}{2R}\right)^2 - 1\right)\left(\frac{\delta^*}{2R} - 2\right) \quad ; \quad \delta^* = R - (R - a(\delta))\cos(\gamma - \beta) \tag{27}$$

where δ^* is the displacement of the symmetry point D (Fig. 9(c)). For a given local indentation δ, the crushing force required for activating the plastic mechanism depicted on Fig. 9(b) is derived by applying the classical theory of beams:

$$P_g(\delta) = \frac{L_1 + L_2}{L_1 L_2}(1 + \xi(\delta))M_0 \tag{28}$$

As shown by (27), $\xi(\delta)$ is a decreasing function of the penetration δ, which explains the decrease of $P_g(\delta)$ before the transition occurring at δ_t (Fig. 9(a)).

As mentioned earlier, a transition is assumed to happen when the local resistance reaches the value required for activating the mechanism of Fig. 9(b). According to (28), the crushing resistance writes at this moment:

$$P_l(\delta_t) = P_g(\delta_t) = \frac{L_1 + L_2}{L_1 L_2}(1 + \xi_t)M_0 \ ; \quad \xi_t = \xi(\delta_t) \tag{29}$$

which means that the global mode is characterized by a central cross-section having a reduced plastic bending moment of $\xi_t M_0$, with $\xi_t = \xi(\delta_t)$.

In order to derive the resistance $P_g(\delta)$ when $\delta > \delta_t$ and to define the displacements during the overall motion of the beam, we consider the situation depicted on Fig. 10(a), where for clarity, the cylinder radius has been intentionally exaggerated in comparison with the vessel size. From this figure, it appears that initially (i.e. for $\delta = 0$), the first contact between the stem $\mathbb{P}$ and the ship occurs at point I. The

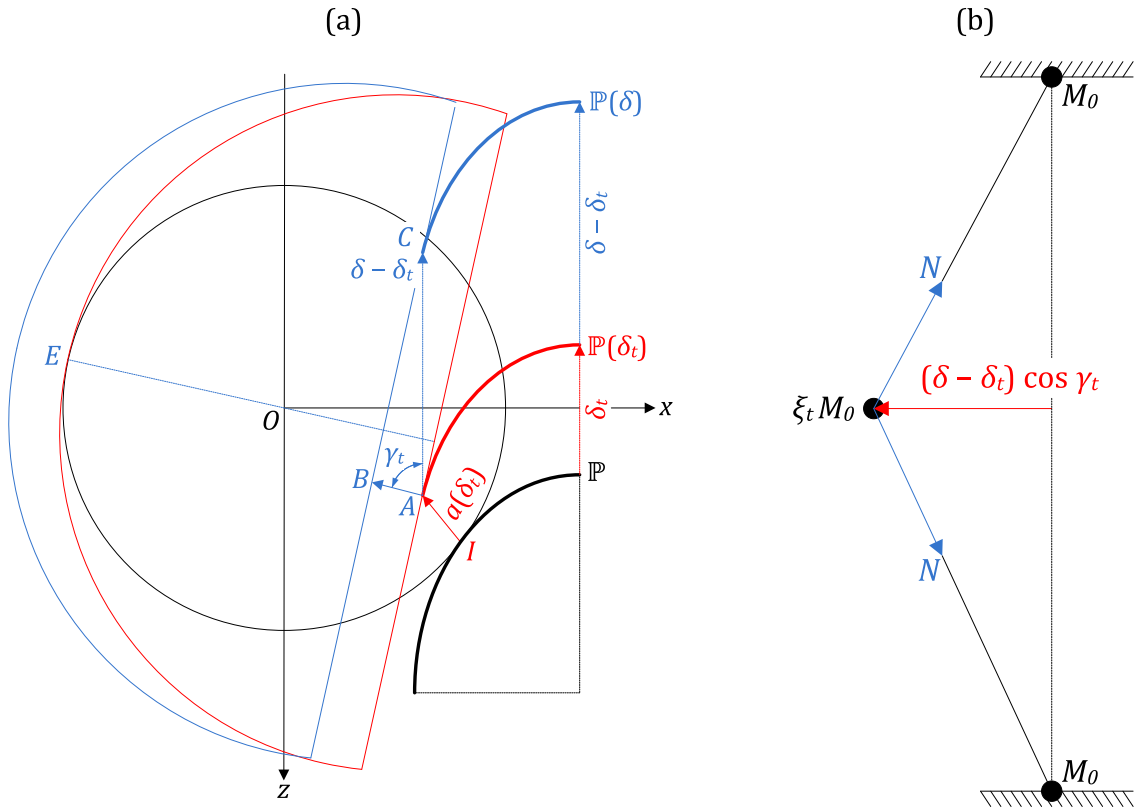

Fig. 10. Displacement of the central section during the global mode.

local mode is then activated, and for $\delta \leq \delta_t$, the section is deformed in accordance with the pattern drawn on Fig. 7(b). When $\delta = \delta_t$, the local resistance $P_l(\delta_t)$ is sufficient for activating the global mode. At this moment, the crushing penetration is $a_t = a(\delta_t)$, the inclination angle is $\gamma_t = \gamma(\delta_t)$ and the approximate plastic bending moment of the corresponding deformed cross-section is equal to $\xi_t M_0$.

When $\delta > \delta_t$, the local crushing process is stopped and the section starts moving as a whole. Fig. 10(a) shows that for a given value of δ, point A is moving to C such that $\overline{AC} = \delta - \delta_t$, which causes the section to move aside. This displacement is characterized by $\overline{AB} = (\delta - \delta_t)\cos\gamma_t$ and the global deforming mode may be studied using the classical beam theory applied to the structure depicted in Fig. 10(b).

During the overall motion represented on Fig. 10(b), the resistance $P_g(\delta)$ comes from both bending and membrane effects. These latter are due to the development of normal tensile forces N associated with the axial lengthening of the beam. A criterion is therefore needed to define how the flexural and extensional contributions are interacting. According to De Oliveira [10], the relation between the bending moment M and the normal force N in the plastic hinges may be written as:

$$M = M_0\left(1 - \frac{N^2}{N_0^2}\right) \quad \text{or} \quad M = \xi_t M_0\left(1 - \frac{N^2}{N_0^2}\right) \tag{30}$$

where $N_0 = 2\pi R\sigma_0 t_p$ is the plastic tensile capacity of the tube. The first of equation (30) is valid for the two extreme cross-sections, while the second has to be applied to the central one. Using this relation and applying the classical beam theory, a closed-form expression of $P_g(\delta)$ is obtained (see Jones [8] for more details):

$$P_g(\delta) = \frac{L_1 + L_2}{L_1 L_2}\left((1+\xi_t)M_0\left(1 - \frac{N(\delta)^2}{N_0^2}\right) + N(\delta)(\delta - \delta_t)\cos\gamma_t\right)$$
$$\text{with}: \quad N(\delta) = \min\left(\frac{N_0^2(\delta - \delta_t)\cos\gamma_t}{2(1+\xi_t)M_0};\ N_0\right) \tag{31}$$

As a conclusion, the resistance $P_v(\delta)$ developed during the impact of a vertical cylinder is calculated by applying equation (26), in which $P_l(\delta)$ and $P_g(\delta)$ are respectively given by (24) and (31).

4. Impact on a horizontal cylinder

4.1. Deformation mechanism

Let us now investigate the particular case of an impact occurring on a horizontal tube, i.e. for which the inclination angle $\zeta = 0$ (Fig. 4). Fig. 11 presents the collision configuration, where the striking vessel is traveling along the line ℓ, making an angle α with the horizontal X axis and strikes the cylinder at a point I defined by its coordinates (X_I,Y_I,Z_I).

$\mathbb{P}$ being the intersection curve between the stem and the horizontal plane located at $Z = Z_I$, it is possible to find a point H such that the tangent line to $\mathbb{P}$ is parallel to the horizontal Y axis. Fig. 11 shows that when the ship is moving along the line ℓ, the points H and I tend to come closer and finally occupy the same position at the beginning of the penetration. At this moment, $\mathbb{P}$ is tangent to the generator g of the cylinder and Fig. 12(a) presents the corresponding configuration in the horizontal plane $Z = Z_I$.

Let us also consider the vertical plane π parallel to (X,Z) and passing through H. The intersection curve Γ between this plane and the stem is not necessarily a straight line, unless $\alpha = 0$. Similarly, when the striking vessel travells along the line ℓ, Γ comes closer to the ring $\mathbb{C}$ of the cylinder and touches $\mathbb{C}$ at point I at the beginning of the impact (Fig. 12(b)).

Fig. 12 shows that closed-form solutions for Y_I, Z_I and X_I may be found by imposing a tangency condition between $\mathbb{P}$ and g, but also between Γ and $\mathbb{C}$. Since the resulting mathematical expressions are quite complex, they are solved numerically by using a Newton–Raphson method.

As the crushing process is concerned, although the impact on a horizontal tube can be treated similarly than the vertical one (Section 3), it is important to account for some particularities. For a given penetration δ, the relative position between the ship and the cylinder is depicted on Fig. 13. Considering the horizontal plane $Z = Z_I$, Fig. 13(a) shows that the current position I' of point I is located at the ordinate $Y_I - \delta\sin\alpha$ and that the displacement of $\mathbb{P}$ along the X axis is only $\delta\cos\alpha$. Consequently, the collision process may be formally modeled by considering that the cylinder section located in the vertical plane $Y = Y_I\sin\alpha$ is simply crushed by the curve Γ with a penetration of $\delta\cos\alpha$, as illustrated on Fig. 13(b).

Comparing Fig. 13(b) with Fig. 7(a), the two situations are seen to be nearly similar but this time the coordinates (X_A,Z_A) of point A have to be derived by calculating the intersection of Γ with the straight line OI. Similarly, the inclination angle γ has also to be found by considering the tangent line d to the curve Γ. The determination of X_A, Z_A and γ may be achieved by assuming that the stem is sufficiently

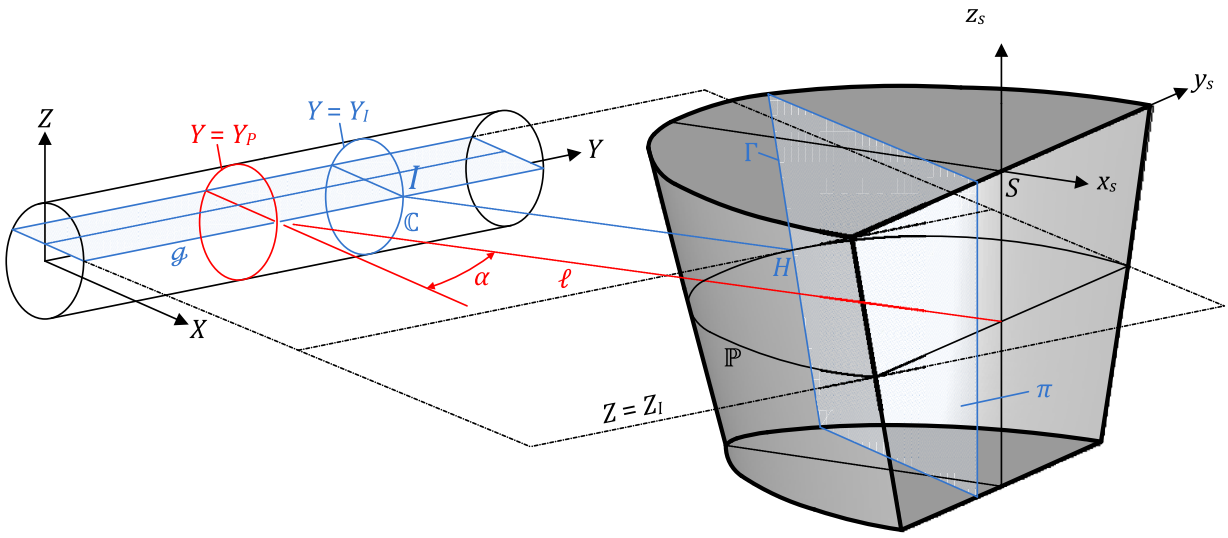

Fig. 11. Collision configuration for an impact on a horizontal cylinder.

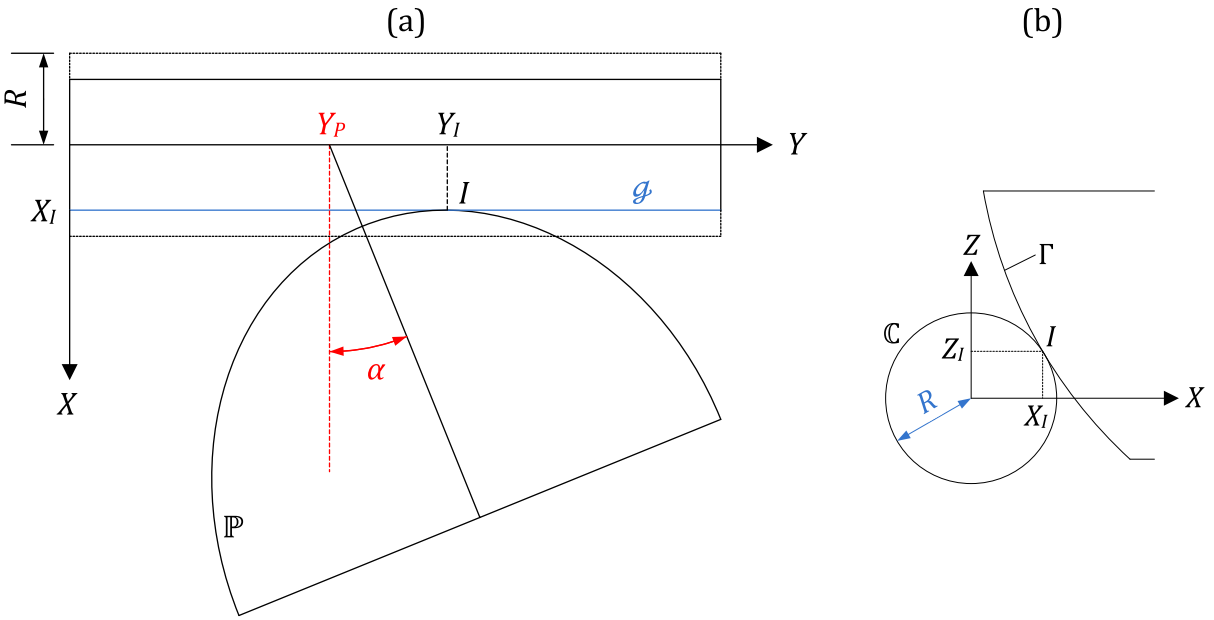

Fig. 12. Initial position of the stem in a horizontal and in a vertical plane.

large to consider Γ as a straight line and therefore very close to d. Consequently, as γ is now constant for all values of δ and equal to the initial inclination β, we simply have the following relations:

$$\gamma = \beta = \text{atan}(X_I/Z_I) \quad ; \quad X_A = X_I - \delta \cos\alpha \sin^2\beta \tag{32}$$

in which the coordinates (X_I,Z_I) are determined from the initial position of the striking vessel. This result allows for the evaluation of the crushing penetration: $a(\delta) = |(X_I - X_A)/\sin\beta|$.

Once γ and $a(\delta)$ have been obtained, it is possible to define how the cylinder cross-section located in the plane $Y = Y_I - \delta\sin\alpha$ is likely to deform. To do so, we can imagine that the deformation pattern of Fig. 7(b) is supposed to be still valid, but this time γ and X_A are evaluated by considering (32) instead of

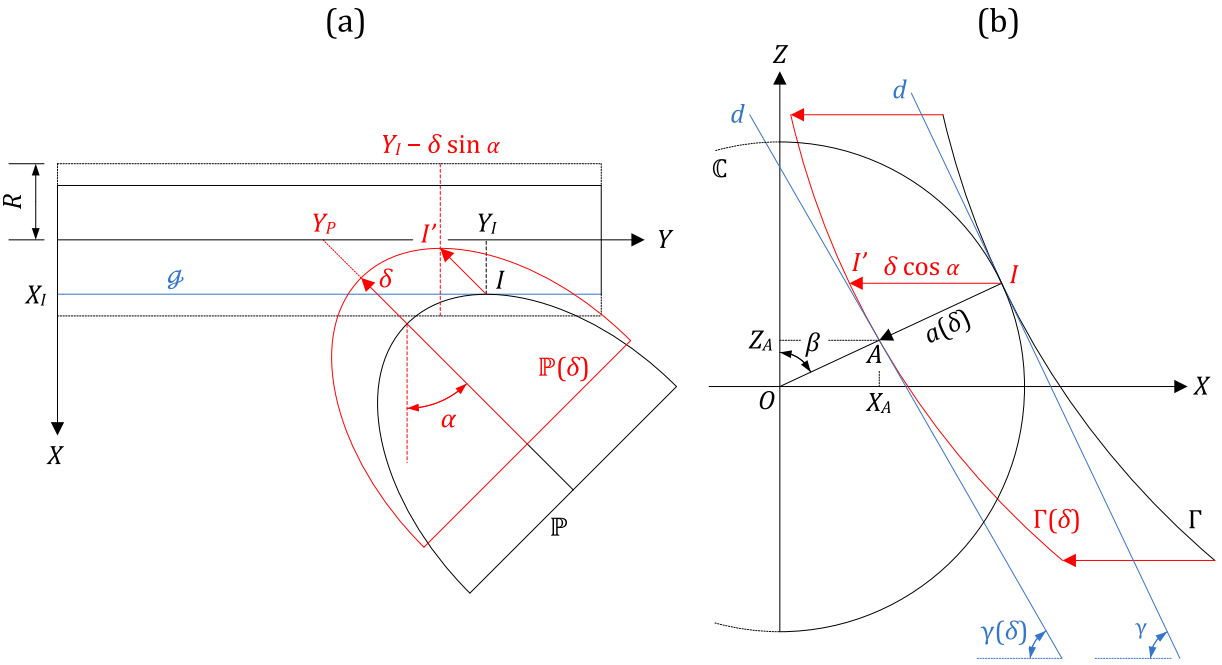

Fig. 13. Relative position of the stem and the tube for a given penetration.

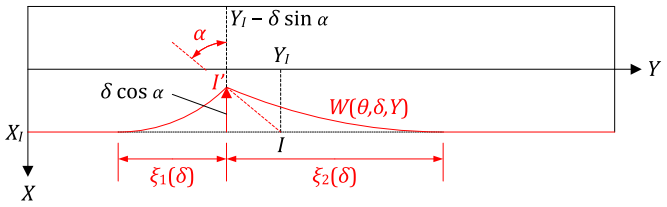

Fig. 14. Extrapolation of the displacement field for any section located along the Y axis.

(4) and (5). The three parameters R_1, R_2 and ψ used for characterizing the crushed section are then given by equations (10), (8) and (11) respectively.

4.2. Definition of the displacement field

As the deformation mechanism of the ring located in the vertical plane $Y = Y_I - \delta\sin\alpha$ is formally identical to the one considered for the case of a vertical cylinder, the displacement field $w(\theta,\delta)$ affecting this cross-section is the same than the one depicted on Fig. 8(a).

Therefore, equation (13) still holds for deriving $w(\theta,\delta)$, but the extrapolation described by (14) to get the velocity $\dot{W}(\theta,\delta,Y)$ over the entire cylinder is not valid anymore. Indeed, if we refer to Fig. 14, the formulas given in (14) have to be modified in the following way:

$$\begin{aligned}
&\dot{W}(\theta,\delta,y) = 0 \quad \text{if} \quad Y \in 0;[Y_I - \delta\sin\alpha - \xi_1(\delta)] \\
&\dot{W}(\theta,\delta,Y) = \dot{w}(\theta,\delta)\left(1 + \frac{Y - Y_I + \delta\sin\alpha}{\xi_1(\delta)}\right) \quad \text{if} \quad Y \in [Y_I - \delta\sin\alpha - \xi_1(\delta);\ Y_I - \delta\sin\alpha] \\
&\dot{W}(\theta,\delta,y) = \dot{w}(\theta,\delta)\left(1 - \frac{Y - Y_I + \delta\sin\alpha}{\xi_2(\delta)}\right) \quad \text{if} \quad Y \in [Y_I - \delta\sin\alpha;\ Y_I - \delta\sin\alpha + \xi_2(\delta)] \\
&\dot{W}(\theta,\delta,y) = 0 \quad \text{if} \quad Y \in [Y_I - \delta\sin\alpha + \xi_2(\delta);\ L]
\end{aligned} \tag{33}$$

Here again, ξ_1 and ξ_2 are two parameters that will be fixed by minimizing the crushing resistance, but it is already clear that we should have $\xi_1 \leq Y_I - \delta\sin\alpha$ and $\xi_2 \leq L - Y_I + \delta\sin\alpha$.

4.3. Local crushing resistance

The evaluation of the crushing resistance may be achieved by following the procedure detailed in Section 3.3. The cylinder may also be considered as a set of horizontal generators slightly connected to vertical circular rings (Fig. 15), so that the total crushing energy rate $\dot{E}$ is still given by equation (15).

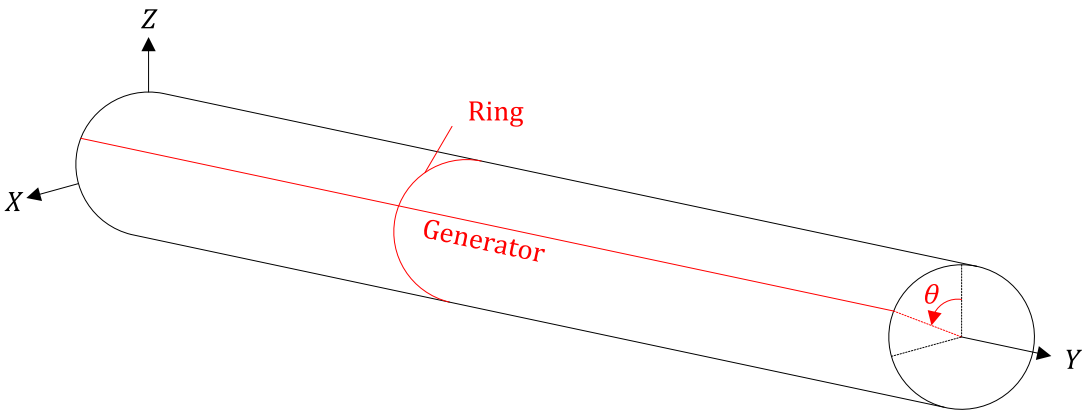

Fig. 15. Ring and generator of a horizontal cylinder.

Furthermore, as $w(\theta,\delta)$ is defined in a similar way than for a vertical tube, the mathematical derivation of $\dot{E}_b$ leads again to equations (16)–(18). The interpolation (19) to get the total contribution of the rings $\dot{E}_r$ is therefore still valid, as it is done in accordance with Fig. 14. Similarly, the total contribution $\dot{E}_g$ of the generators is also given by expression (22) and equation (23) is also used to get $\dot{E}$. Once the internal energy has been calculated, the virtual work principle is applied. This latter states that $\dot{E}$ has to be equated to the external work rate of the crushing resistance $P_h(\delta)$. As depicted on Fig. 13(b), for a given penetration δ, the contact point is moving from I to A, so that the corresponding work rate performed by $P_l(\delta)$ is simply $P_l(\delta)\dot{a}(\delta)$. Therefore, by accounting for (32), we have:

$$\begin{aligned} &P_l(\delta)\dot{a}(\delta) = \dot{E}_b\frac{\xi_1+\xi_2}{2} + \left(\frac{1}{\xi_1}+\frac{1}{\xi_2}\right)\dot{E}'_m \\ \Leftrightarrow &\mathrm{P_l}(\delta) = \left(\mathrm{E_b}\frac{\xi_1+\xi_2}{2} + \left(\frac{1}{\xi_1}+\frac{1}{\xi_2}\right)\mathrm{E'_m}\right)\Big/\sin\beta\cos\alpha \end{aligned} \tag{34}$$

The derivation of ξ_1 and ξ_2 is achieved by minimizing (34), so expression (25) have to be corrected to account for the obliquity of the impact:

$$\xi_1(\delta) = \min\left(\sqrt{E'_m/E_b};\ Y_I - \delta\sin\alpha\right); \xi_2(\delta) = \min\left(\sqrt{E'_m/E_b};\ L - Y_I + \delta\sin\alpha\right) \tag{35}$$

This final equation may be used in conjunction with (19), (22) and (34) to get $P_l(\delta)$, but this has to be done in accordance with the particularities detailed in (32) for $\zeta = 0$.

4.4. Global crushing resistance

The derivation of the resistance $P_g(\delta)$ during the global deforming mode for a horizontal cylinder can be performed by following the same procedure than the one described in Section 3.4. For a given value of δ, the plastic mechanism related to the overall motion of the cylinder is depicted on Fig. 16(a), where the central plastic hinge is also characterized by a lower plastic bending moment $\xi(\delta)M_0$.

As for the case of a vertical tube, the reduction coefficient $\xi(\delta)$ may be found by applying (27), but we should account here for the particular definition of $a(\delta)$ as detailed in (32):

$$\xi(\delta) = \frac{1}{2}\left(\left(\frac{\delta\cos\alpha\sin\beta}{2R}\right)^2 - 1\right)\left(\frac{\delta\cos\alpha\sin\beta}{2R} - 2\right) \tag{36}$$

Similarly, for a given value of δ, the global resistance required to activate the plastic mechanism of Fig. 16(a) can be calculated by modifying (28) to account for the inclination angle α. Therefore, in equation (28), L_1 and L_2 simply have to be replaced by $Y_I - \delta\sin\alpha$ and L_2 by $L - Y_I + \delta\sin\alpha$ to get the following result:

$$P_g(\delta) = \frac{L\sin\beta}{(Y_I - \delta\sin\alpha)(L - Y_I + \delta\sin\alpha)}(1+\xi(\delta))M_0 \tag{37}$$

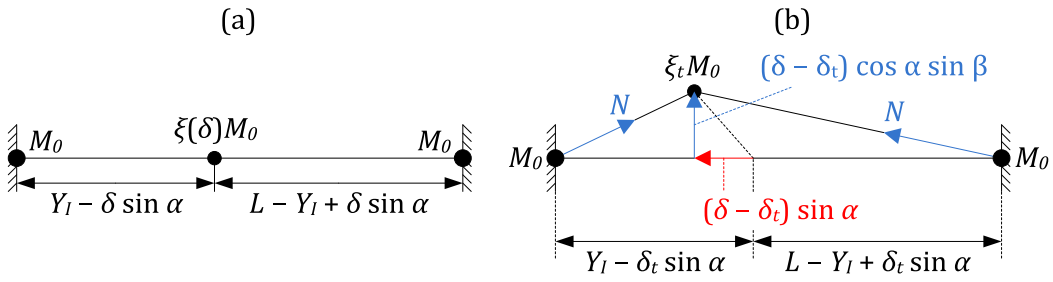

Fig. 16. Global plastic mechanism for a horizontal cylinder.

The transition from local to global deforming mode occurs when $\delta = \delta_t$. At this moment, the local crushing resistance is equal to the global one calculated by applying (37):

$$P_l(\delta_t) = P_g(\delta_t) = \frac{L \sin\beta}{(Y_I - \delta_t \sin\alpha)(L - Y_I + \delta_t \sin\alpha)}(1+\xi_t)M_0 \;\; ; \quad \xi_t = \xi(\delta_t) \tag{38}$$

which means that the value reached by $P_l(\delta)$ is sufficient for activating the global mode depicted on Fig. 16(a). Once the transition has occurred, i.e. when $\delta > \delta_t$, the resistance $P_g(\delta)$ is no longer given by (37) because normal tensile forces N appear inside the two arms of the deforming beam (Fig. 16(b)). In fact, when the structure is forced into the overall motion, an axial lengthening is added to the bending effects. In the vertical case, the main difficulty is to account for the oblique trajectory followed by the vessel ($\alpha \neq 0$). This problem has been treated by some authors, such as Tin Loi [12] or Buldgen [13]. By following the approximate theoretical procedure described in Ref. [13] for example, it is possible to establish the subsequent results:

$$\begin{aligned} P_g(\delta) &= \frac{L\sin\beta}{\ell_1(\delta)\ell_2(\delta)}\left(M_0(1+\xi_t)\left(1-\frac{N(\delta)^2}{N_0^2}\right)+N(\delta)(\delta-\delta_t)\cos\alpha\sin\beta\right) \\ \text{with}: \quad N(\delta) &= \frac{N_0^2}{2(1+\xi_t)M_0}\frac{(\delta-\delta_t)\cos\alpha\sin\beta}{2}\left(1+\frac{\ell_1(\delta)\ell_2(\delta)L}{\ell_1(\delta_t)\ell_2(\delta)^2+\ell_2(\delta_t)\ell_1(\delta)^2}\right) \\ \ell_1(\delta) &= Y_I - \delta\sin\alpha \;\; ; \quad \ell_2(\delta) = L - Y_I + \delta\sin\alpha \end{aligned} \tag{39}$$

As a conclusion, the crushing resistance $P_h(\delta)$ of a horizontal cylinder during the collision may be derived in the same way than (26), but $P_l(\delta)$ and $P_g(\delta)$ have to be calculated by applying (34) and (39) respectively.

5. Impact on an oblique cylinder

5.1. Crushing resistance

It is quite difficult to handle with the mathematical expressions of the stem and of the cylinder in the oblique case. Indeed, when $\zeta \neq 0$ and $\zeta \neq \pi/2$, it is difficult to postulate a consistent displacement field $W(\theta,\delta,y)$ representative of the cross-section deformation during the crushing process. The main difficulty comes from the fact that the rings have an elliptic shape and not a circular one (Fig. 17), so it is not easy to imagine how this section is likely to deform when it is impacted by the stem.

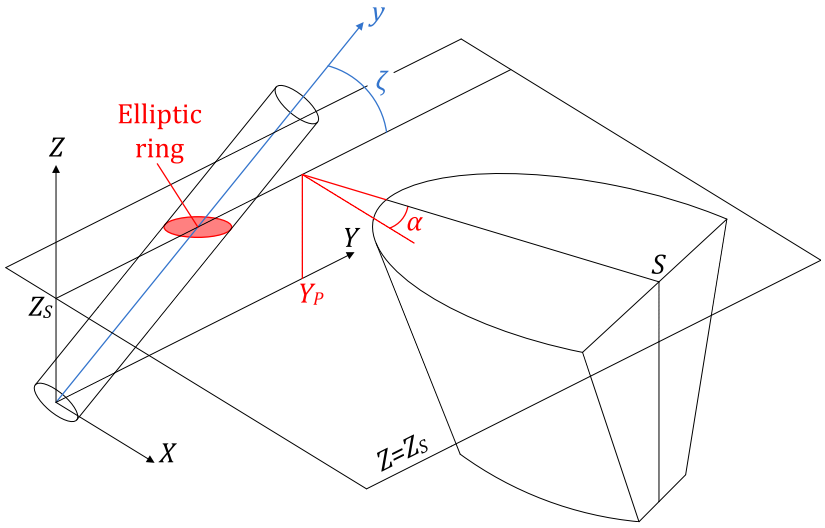

Fig. 17. Configuration of an oblique impact occurring on an inclined cylinder.

Table 1
Properties of the two cylinders used for the numerical simulations.

Property	Notation	Unit	Leg	Brace
Radius	R	m	0.65	0.35
Length	L	m	10	8
Thickness	t_p	m	0.038	0.0127
Inclination	ζ	deg	60;90	0;30;45

Solving such a problem is not the purpose of this paper. Nevertheless, in order to evaluate the crushing resistance $P(\delta)$ in the case of an oblique cylinder, we will simply admit that this one can be calculated by performing a linear interpolation between the two particular solutions $P_v(\delta)$ and $P_h(\delta)$ derived in Sections 3 and 4. In other words, we postulate that:

$$P(\delta) = \left(1 - \frac{2\zeta}{\pi}\right) P_h(\delta) + \frac{2\zeta}{\pi} P_v(\delta) \tag{40}$$

5.2. Numerical validation

In order to validate the mathematical developments exposed in the previous sections, we can check if the theoretical prediction $P(\delta)$ given by (40) is in accordance with numerical solutions. To do so, some numerical simulations are carried out using the finite element software LS-DYNA. Two different cylinders, whose properties are listed in Table 1, are studied. For the first one, typical dimensions of a jacket leg are considered, while the second may be assimilated to a classical brace. Only two different inclinations (60° and 90°) are considered for the leg because it is quite uncommon to have $\zeta < 60°$ for this kind of structure. Similarly, for the brace, it seems reasonable to keep ζ lower than 45°. Both cylinders are supposed to be perfectly restrained at their extremities.

For the purpose of numerical simulations, the leg and the brace are respectively modeled with 9100 and 7040 Belytschko-Tsay shell elements (see reference [14] for more details). The mesh is regular, with an average element dimension of 5 cm × 5 cm. The material elastic–plastic behavior is described by the bilinear stress–strain curve depicted on Fig. 18 and by using the properties listed in Table 2. At the end of the elastic phase (i.e. for $\sigma = \sigma_0$), the material is submitted to a slow hardening characterized by the tangent modulus E_T. In reality, this phase ends by the rupture of the material, which is not considered in the present paper.

These two cylinders are impacted by a stem assumed to be perfectly rigid. The main dimensions of the striking vessel are presented in Table 3, with the notations introduced on Fig. 4. The ship is modeled using 23012 Belytschko-Tsay shell elements [14] and the mesh is refined near the impact area in order to ensure good contact conditions with the tube.

The relative position between the stem and the cylinder is defined by the parameters (Y_P;Z_S;α), as depicted on Fig. 4. In order to check the validity of equation (40), different configurations associated with various values have been investigated.

5.2.1. Impact on a leg

A lot of numerical simulations were performed in order to assess the crushing resistance of a leg for different values of ζ, α, Y_P and Z_S. For conciseness, all the obtained results will not be presented here but

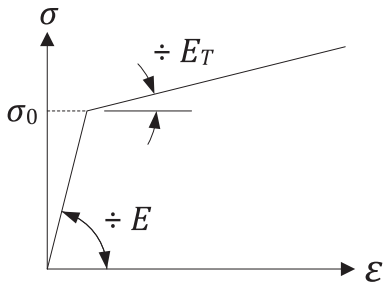

Fig. 18. Stress–strain curve used for the numerical simulations.

Table 2
Material law used for the numerical simulations.

Property	Notation	Value
Young modulus	E	210,000 MPa
Poisson ratio	ν	0.3
Flow stress	σ_0	240 MPa
Tangent modulus	E_T	1018 MPa

Table 3
Main dimensions of the striking vessel.

Property	Notation	Unit	Value
Elliptic radius 1	p	m	6
Elliptic radius 2	q	m	8
Total height	h_b	m	7
Stem angle	ϕ_b	deg	78
Side angle	ψ_b	deg	74

only the five scenarios described in Table 4. For the case of a vertical cylinder ($\zeta = 90$), there is no need to specify a value for α because the impact problem is axisymmetric.

For each scenario, the curves showing the evolution of $P(\delta)$ as predicted by (40) are compared on Figs. 19–23 together with the ones calculated by LS-DYNA. The simulations were arbitrarily stopped after reaching a penetration of 1 m. These figures show a quite good accordance between numerical and analytical results. Moreover, in almost all cases, the analytical derivation was found to be conservative as it tends to underestimate the crushing resistance. In fact, the maximal discrepancy was observed for scenario 2.1 (Fig. 22), for which an underestimation of 25% of $P(\delta)$ was found when $\delta = 1$ m. This may be explained by the fact that the theoretical model tends to activate the global mode a bit too early.

As shown by some of the above figures, the slope of the analytical curve may change suddenly, reflecting the transition from the local to the global deforming mode. Indeed, it is worth recalling that the theoretical models first postulate a local crushing of the cylinder. During this phase, the rigidity is quite important and explains why the force is rapidly growing. This denting process ends with the development of an overall bending motion of the cylinder, which is a more flexible deformation process and is responsible for an inflection of the resistance curve. This change in the tube behavior may be illustrated by Fig. 24, which presents some results obtained numerically with LS-DYNA. Fig. 24(a) shows the deformation of a cylinder cross-section located near the initial contact point. For a given penetration δ of the striking vessel, a global backward movement (quantified by δ_g) occurs. Fig. 24(b) presents two different top views of the tube. On the upper one, the total indentation δ is quite small, so the crushing process is only characterized by a local denting δ_l, the rear edge of the tube remaining straight. The lower figure is obtained for a larger value of δ and shows that the global mode has already been activated.

5.2.2. *Impact on a brace*

We also performed a great number of collisions involving the brace and the vessel described above. Nevertheless, for conciseness, we will only present the results obtained for the scenarios listed in Table 5. The corresponding curves are depicted on Figs. 25–27.

Table 4
Collision configurations for an impact on a leg.

Scenario	ζ (deg)	α (deg)	Y_P (m)	Z_S (m)
1.1	60	0	3	6
1.2	60	30	1	6
1.3	60	45	−1	5
2.1	90	/	0	6
2.2	90	/	4	6

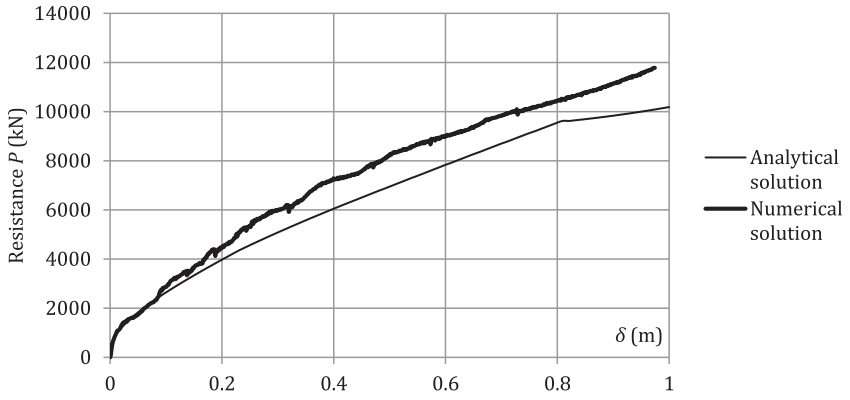

Fig. 19. Comparison of the analytical leg resistance to the numerical one for scenario 1.1.

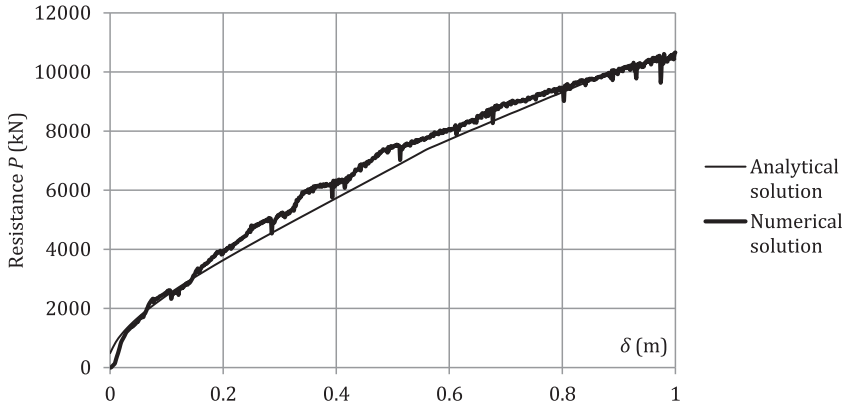

Fig. 20. Comparison of the analytical leg resistance to the numerical one for scenario 1.2.

As shown by these figures, the conclusions drawn for a leg are also valid for a brace. Here again, the agreement between analytical and numerical solutions seems to be satisfactory. Moreover, in all the cases, the theoretical approximation tends to be conservative. The maximal discrepancy is equal to 25% and is observed for scenario 3 (Fig. 25).

As for to the case of an impact on a leg (Section 5.2.1), the sudden slope change appearing on the analytical curves is also due to the theoretical transition from the local to the global resisting mode. It is worth noting that this switch is occurring sooner for braces because of a smaller radius R compared with the legs one.

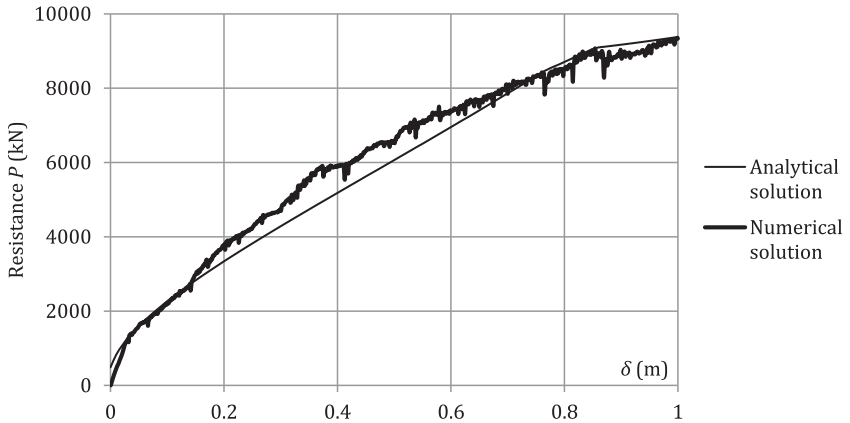

Fig. 21. Comparison of the analytical leg resistance to the numerical one for scenario 1.3.

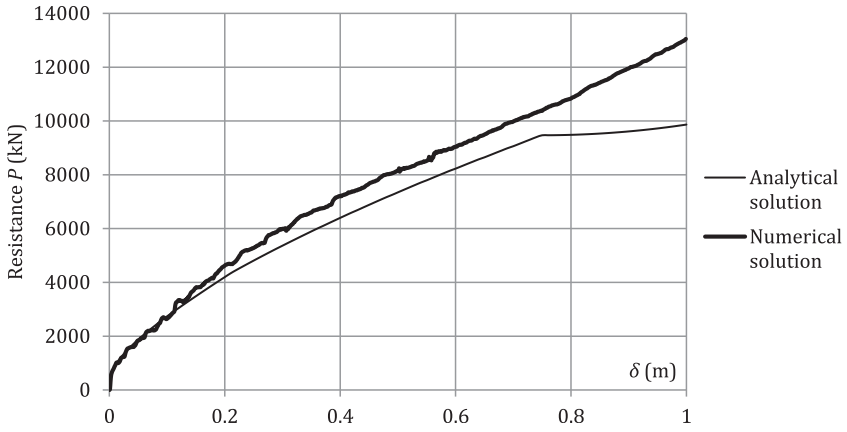

Fig. 22. Comparison of the analytical leg resistance to the numerical one for scenario 2.1.

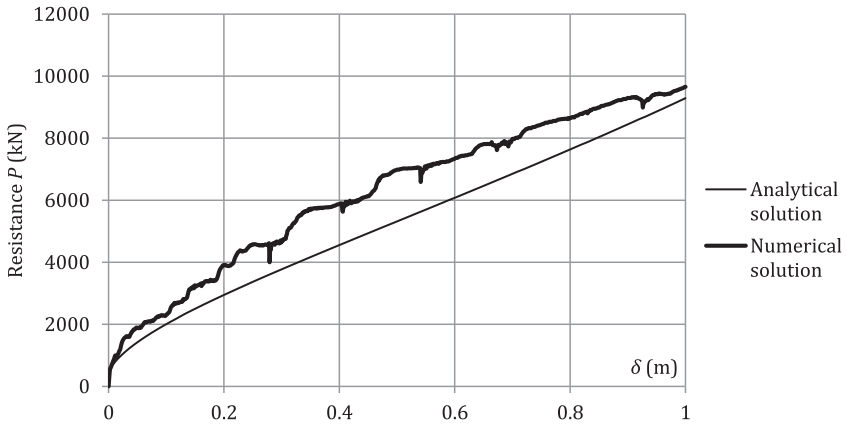

Fig. 23. Comparison of the analytical leg resistance to the numerical one for scenario 2.2.

6. Impact on a full-scale jacket

In order to have a better insight of what happens during an impact on a wind turbine, the finite elements software LS-DYNA was used to simulate a collision occurring near the top of the structure (Fig. 28). The tubes constituting the jacket are modeled with Belytschko-Tsay shell elements [14] associated with an elastic–plastic material law described by a similar curve than the one of Fig. 18. The four legs are supposed to be perfectly clamped in the ground and the top of the jacket is considered as a perfectly rigid element in order to account for the presence of the platform.

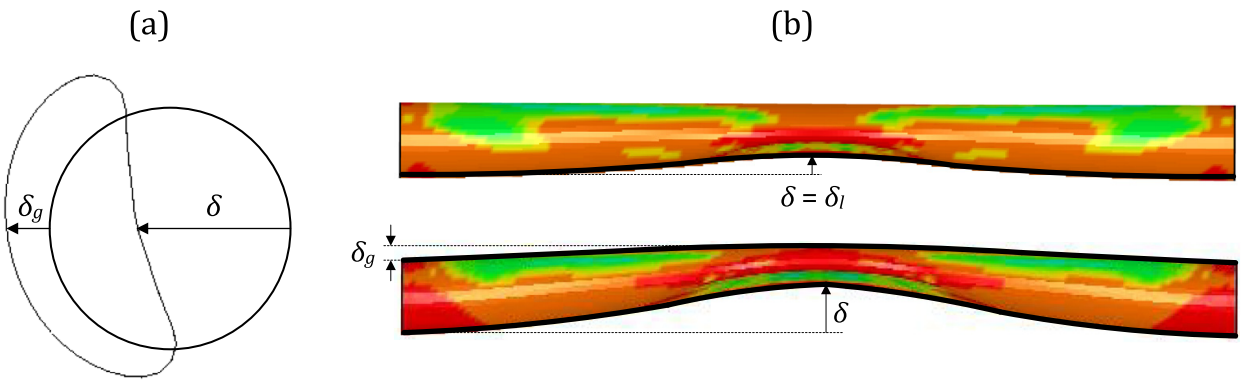

Fig. 24. Local and global deforming modes.

Table 5
Collision configurations for an impact on a brace.

Scenario	ζ (deg)	α (deg)	Y_P (m)	Z_S (m)
3	0	45	−1	1
4	30	30	1	5
5	45	0	2	6

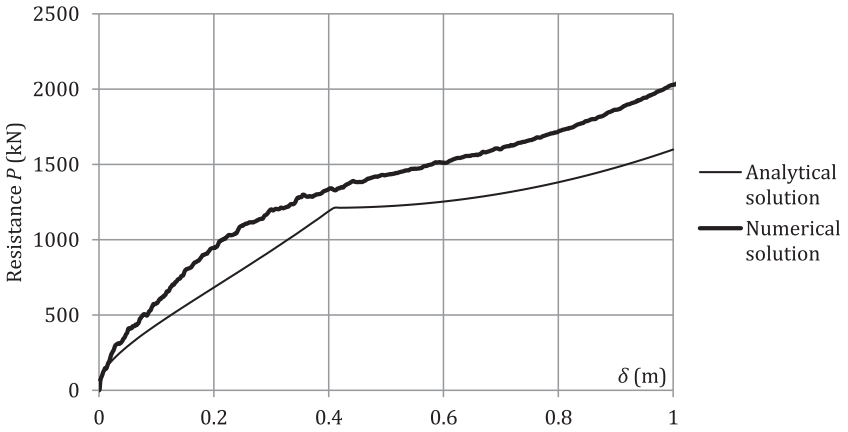

Fig. 25. Comparison of the analytical brace resistance to the numerical one for scenario 3.

The striking stem is considered as being perfectly rigid, which implies that all the collision energy is dissipated by the support. Its total mass is close to 5000 tons and two different initial velocities of 2 m/s and 5 m/s are used for the simulations. The contact with the jacket is modeled by using the AUTOMATIC_GENERAL_SURFACE_TO_SURFACE penalty contact algorithm of LS-DYNA [14].

For an initial striking velocity of 2 m/s, only the leg is impacted by the stem (see Fig. 28). In order to obtain a rapid estimation of the crushing resistance, the simplified method described previously is applied by assuming that the collision takes place on an individual cylinder *AB* characterized by the geometrical parameters introduced on Fig. 4. Applying the above-mentioned mathematical approach to this isolated tube, the resistance $P(\delta)$ is assessed for each value of the vessel penetration δ. This is achieved by applying the interpolation formula (40) and leads to the analytical curve shown Fig. 29(b). Similarly, the internal energy dissipated by the cylinder is also computed, as depicted on Fig. 29(a). If we compare the present analytical curves with the ones given by LS-DYNA, we see from Fig. 29 that the agreement is quite satisfactory.

Let us now investigate the case of an initial striking velocity of 5 m/s. In such a scenario, both the leg and the brace of Fig. 28 are impacted by the rigid stem. Once again, these cylinders can be seen as isolated elements and equation (40) may be applied to get an approximation of the collision resistance.

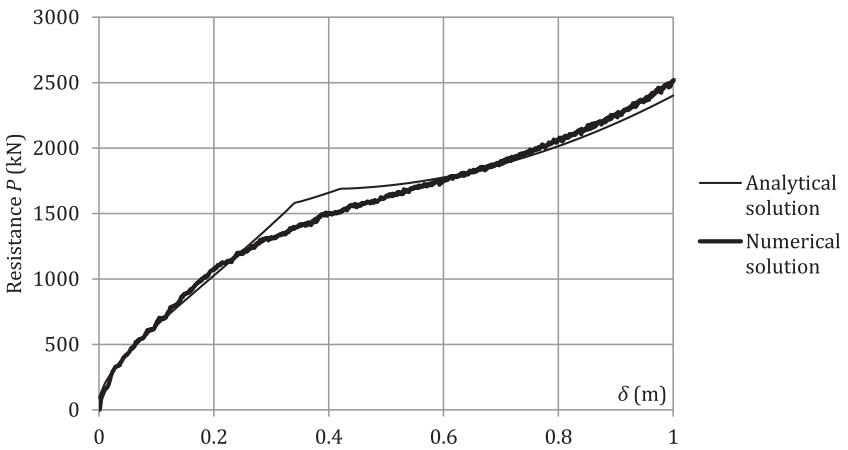

Fig. 26. Comparison of the analytical brace resistance to the numerical one for scenario 4.

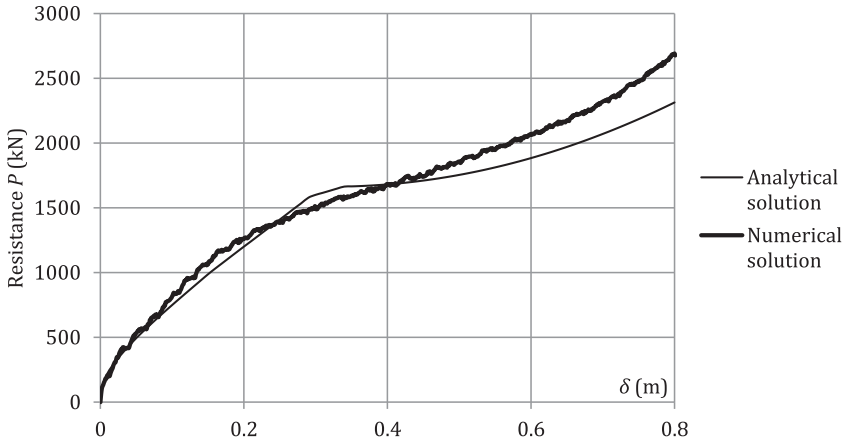

Fig. 27. Comparison of the analytical brace resistance to the numerical one for scenario 5.

Doing so leads to the curves presented on Fig. 30. This time, there is a large discrepancy with the numerical solution given by LS-DYNA, as the theoretical model drastically overestimates the energy dissipation and the collision resistance.

This important divergence may be explained by the boundary conditions assumed for the analytical derivation. Indeed, as detailed in the previous sections, we consider that both extremities of the cylinder are strongly clamped and therefore do not move during the collision. In other words, the hypothesis is made that the nodes *A*, *B* and *C* of Fig. 28 are fixed. Nevertheless, this is obviously not the case as the jacket is also forced into an overall flexural and torsional movement (Fig. 31). For the smaller velocity of 2 m/s, these motions remains quite small, which explains the quite good agreement.

This particular point may be investigated in more details by comparing the reaction forces at the extremities of *AB* (Fig. 28) with those derived by working on the same isolated cylinder. The curves showing the evolution of the forces along the *x* and *y* axes are plotted on Figs. 32 and 33 for the upper and lower supports respectively (point *A* and *B* on Fig. 28).

As the upper support is concerned (point *A* on Fig. 28), the results reported on Fig. 32 show that the slopes of the reaction forces are similar. As expected, the reaction force magnitudes for an isolated cylinder are greater than those obtained for the full-scale jacket model. This may be simply explained by the more important flexibility of the supports in this last case. Moreover, as depicted on Fig. 32(b),

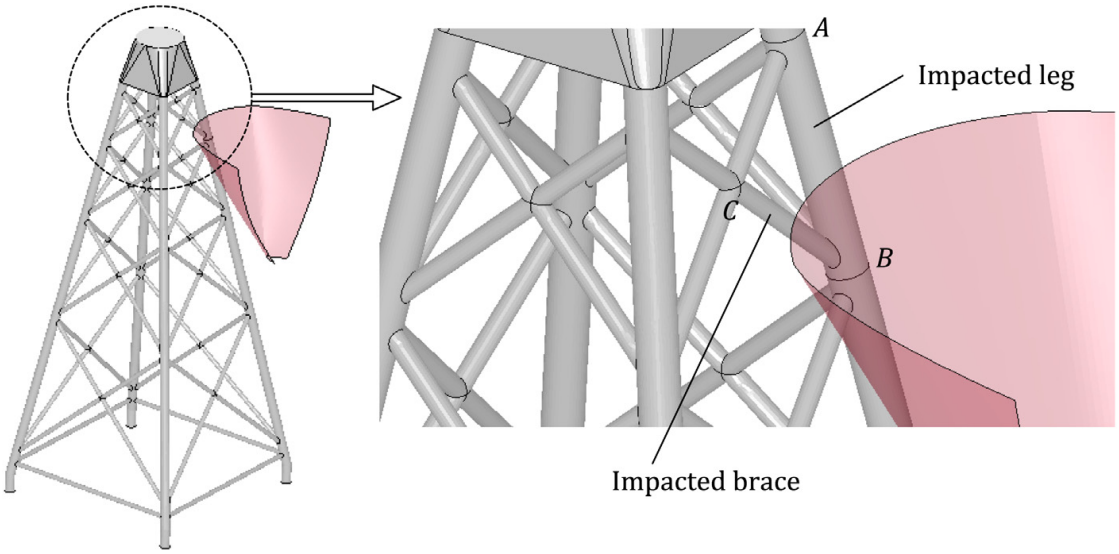

Fig. 28. Collision scenario for the impact on a full-scale jacket.

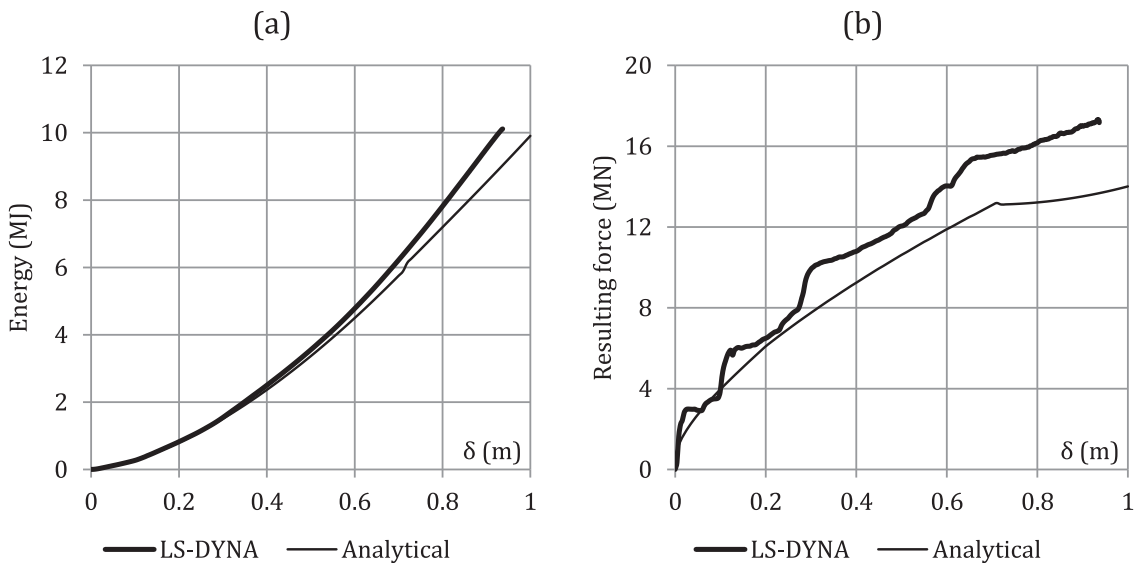

Fig. 29. Comparison of (a) the internal energy and (b) the total crushing force obtained analytically and numerically for an initial velocity of 2 m/s.

there is stabilization of the *y* reaction when the contact with the brace *BC* (Fig. 28) occurs. Of course, this is not taken into account when working with an isolated cylinder.

Similar conclusions may be drawn for the lower support (point *B* on Fig. 28) when analyzing Fig. 33. Nevertheless, it is worth mentioning that the *x* and *y* reactions for the isolated cylinder tend to infinity when the penetration reaches the value of 1.5 m. This is particularly visible on Fig. 33(b) and may be justified by the fact that the striking vessel enters in contact with the lower support. As this latter is assumed to be perfectly fixed in this case, the reaction forces increase therefore drastically.

As a conclusion of this analysis, working with an isolated cylinder tends to overestimate the reaction forces to some extent because the actual flexibility of the supports is not correctly modeled. Of course, this approach becomes irrelevant as soon as one the bow is reaching of the supports.

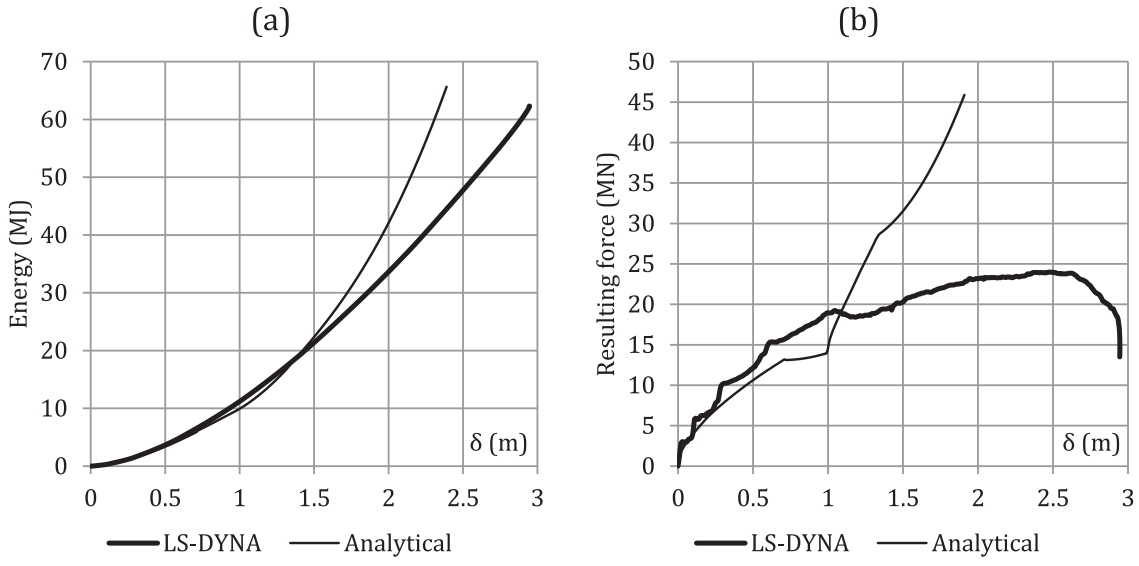

Fig. 30. Comparison of (a) the internal energy and (b) the total crushing force obtained analytically and numerically for an initial velocity of 5 m/s.

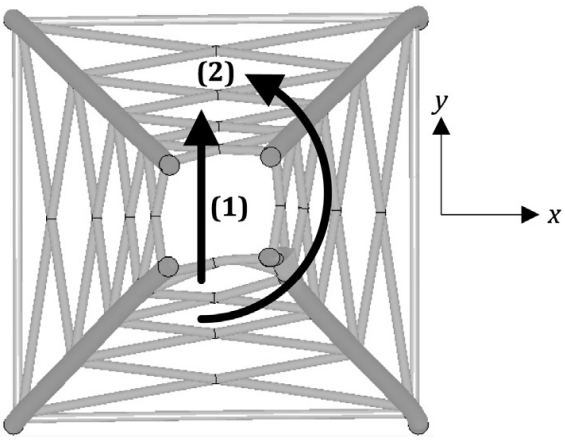

Fig. 31. Overall flexural (1) and torsional (2) movement of the jacket for a velocity of 5 m/s.

7. Future work

The numerical simulations performed on a full-scale jacket show that the analytical model presented in this paper is not sufficient and does not entirely reflect all the phenomena involved in the collision process.

A first point to investigate is the *coupling* that is likely to appear between the different tubes constituting the jacket. In the present model, only the cylinders that are directly in contact with the striking vessel are assumed to be crushed (Fig. 34(a)), but it is clear that the adjacent ones may also deform even though they have not been impacted (Fig. 34(b)). In other words, our theoretical approach is not able to account for the displacements affecting each node of the wind turbine support, but this can be achieved in a similar way than the one followed by Paik [15] for stiffened plates. This methodology is already implemented in the USFOS software developed by the company SINTEF Marintek and the Norwegian University of Science and Technology (NTNU). Consequently, the future work will aim to integrate the new developments exposed in this paper into a general calculation code able to capture the overall motions of the structure.

Another point to consider is the *ground flexibility*. In the numerical simulations presented in Section 6, the four jacket legs were assumed to be perfectly clamped in the ground, which is not necessarily

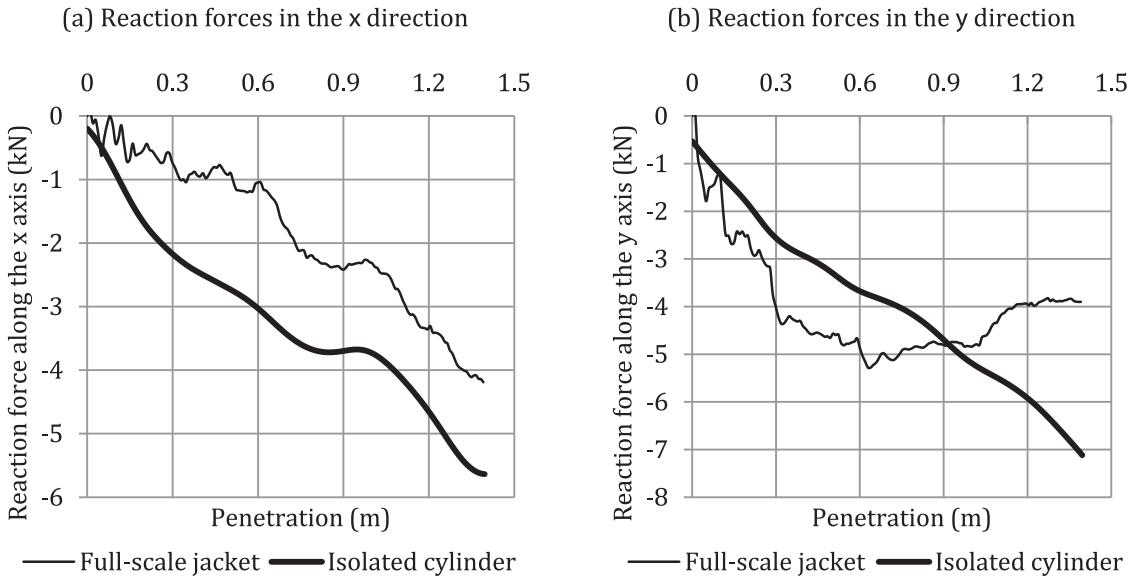

Fig. 32. Evolution of the reaction forces with the penetration for the upper support.

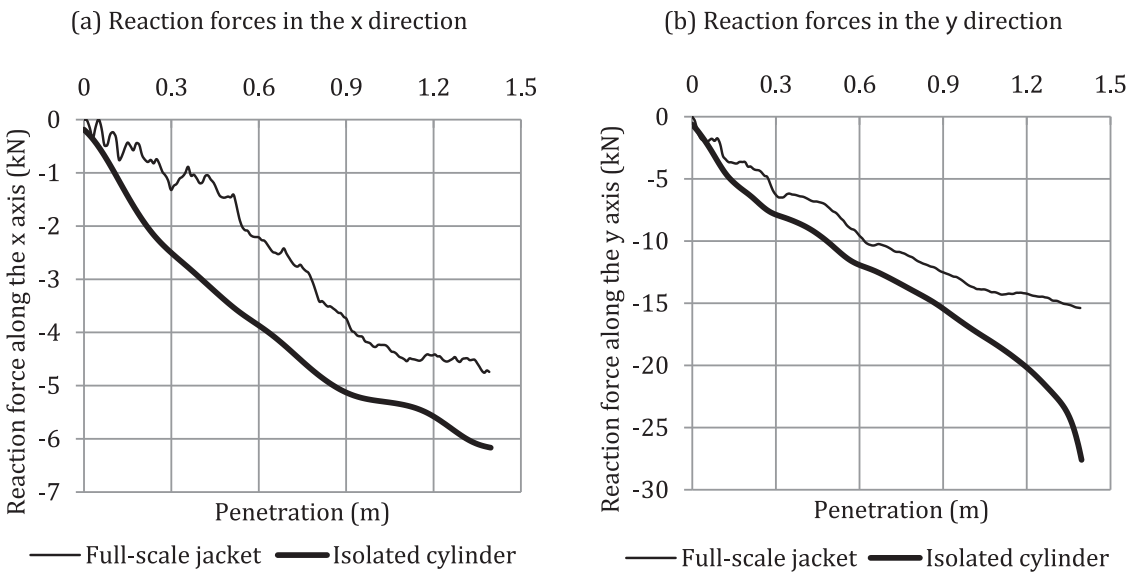

Fig. 33. Evolution of the reaction forces with the penetration for the lower support.

realistic as the ground does not have an infinite rigidity. This should be carefully investigated, by fixing each leg with extensional and rotational springs (Fig. 34(c)). These latter have to be calibrated to reflect the soil flexibility. This will be also a matter for future work.

Finally, the last point to discuss is the effect of the *actual vessel strength*. As considering a perfectly rigid vessel is often too conservative, a sensitivity analysis of the jacket crashworthiness to the striking ship bow deformability has also been performed and will be presented in an upcoming paper of Le Sourne et al. [11].

8. Conclusion

In this paper, a closed-form expression for evaluating the resistance opposed by an inclined tube submitted to a collision with the stem of a given ship is developed. This is done by accounting for the shape of the flare and for different collision angles.

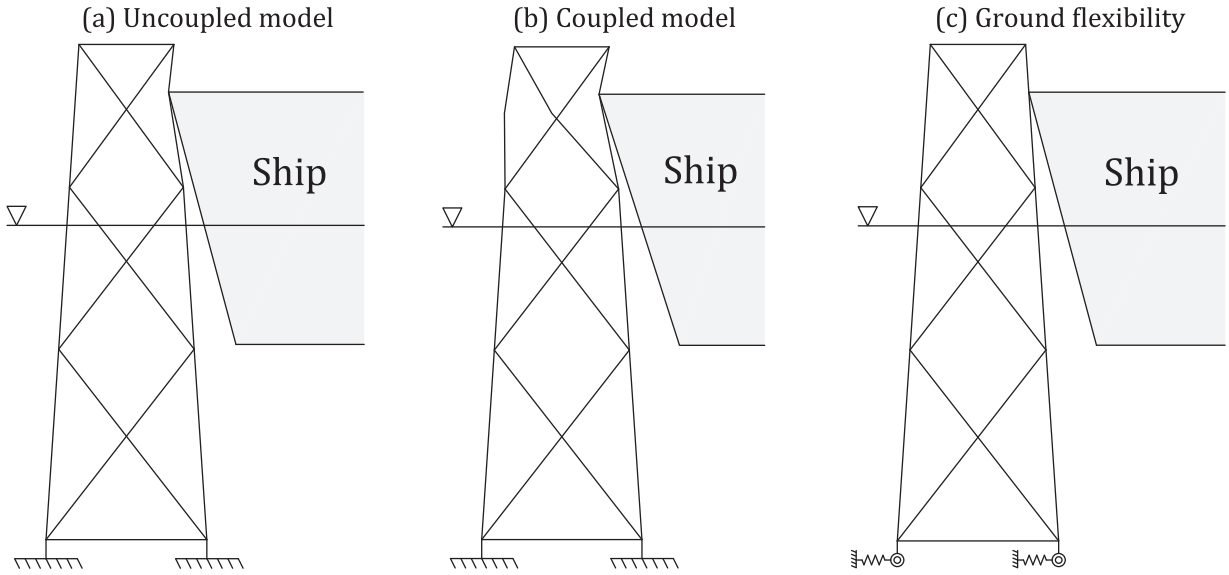

Fig. 34. Further investigations.

As a first step, the particular case of an impact occurring on a vertical cylinder is investigated. The analytical derivation is performed by applying the upper-bound method. To do so, we first imagine a displacement field that is compatible with the assumed shape of the striking vessel. To evaluate the impact resistance, the tube is idealized by a set of horizontal rings slightly connected to vertical generators. Both of them are submitted to an assumed displacement profile and the virtual velocities principle is applied to get the corresponding crushing resistance.

As a second step, the situation of a horizontal cylinder is treated. The method is similar to the vertical case, but the assumed deformation pattern is of course somewhat different.

Finally, an interpolation formula is proposed to evaluate the crushing resistance for any inclination of the tube. In order to validate the theoretical developments, the crushing force assessed analytically is compared with numerical results. More than fifty different collision situations were investigated and some of them are presented in this paper. In almost all the cases, the agreement between our simplified method and the results given by the finite elements code LS-DYNA are satisfactory, as the divergence never exceeds 25%. Moreover, the analytical procedure leads to conservative results, as the crushing force and the energy dissipated by the cylinder are always underestimated.

In the last part of this paper, an impact on a full-scale jacket is briefly treated. Once again, the collision is simulated using LS-DYNA and the corresponding results are compared with the analytical predictions. The numerical simulations are performed by considering two different initial velocities for the striking vessel, i.e. 2 m/s and 5 m/s. In the first case, when the velocity is sufficiently low, the agreement of the present theoretical derivation is quite satisfactory. Nevertheless, in the second case, when the velocity is increased, a non-negligible divergence is observed. This one is due to the fact that the tubes surrounding the impacted one are also deformed during the crash. This points out the necessity of accounting for a coupling between all the super-elements, which is not done so far in our simplified method. So there is still a need for further work that should be performed during upcoming years.

Acknowledgments

This work has been performed in the frame of the research project “CHARGEOL”. The authors would like to thank the region “Pays de la Loire” for its financial support but also STX France and Bureau Veritas for their technical participation in defining the scope of work.

References

[1] Amdahl J, Holmas T. High energy ship collisions with jacket supported offshore wind turbines. In: Proceedings of the international conference on computational methods in marine engineering, Barcelona, Spain; 2011.
[2] Vredeveldt AW, Schipperen JHA, Nassar QHA, Spaans CA. Safe jacket configurations to resist boat impact. In: Leira J, editor. Collision and grounding of ships and offshore structures; 2013. London.
[3] Biehl F. Collision safety analysis of offshore wind turbines. In: 5th LS-DYNA Anwenderforum, Bamberg, Germany; 2005.
[4] Amdahl J, Johansen A. High-energy ship collision with jacket legs. In: Proceedings of the 11th international offshore and polar engineering conference, Stavanger, Norway; 2001.
[5] Hoo Fatt MS, Wierzbicki T. Damage of plastic cylinders under localized pressure loading. Int J Mech Sci 1991;33:999–1016.
[6] Wierzbicki T, Suh MS. Indentation of tubes under combined loading. Int J Mech Sci 1988;30:229–48.
[7] Zeinoddini M, Harding JE, Parke GAR. Effect of impact damage on the capacity of tubular steel members of offshore structures. Mar Struct 1998;11:141–57.
[8] Jones N. Structural impact. Cambridge: Cambridge University Press; 1997.
[9] Suh MS. Plastic analysis of dented tubes subjected to combined loading. Cambridge: Massachusetts Institute of Technology, Department of Ocean Engineering; 1987 [Ph. D. thesis].
[10] de Oliveira J, Wierzbicki T, Abramowicz W. Plastic behavior of tubular members under lateral concentrated load. DNV Technical Report n°82-0708; 1982.
[11] Le Sourne H, Barrera A, Maliakel J.B. Numerical crashworthiness analysis of an offshore wind turbine jacket impacted by a ship. Submitted to J Mar Sci Technol.
[12] Tin Loi F. Post-yield behavior of a rigid-plastic beam with partial axial and rotational end fixities. Int J Mech Sci 1990;32:623–30.
[13] Buldgen L, Le Sourne H, Rigo P. Fast strength assessment of mitre gates to ship impact. Int J Crashworthiness 2013;18:423–43.
[14] Hallquist JO. LS-DYNA theoretical manual. Livermore Software Technology Corporation; 2006.
[15] Paik JK, Thayamballi AK. A concise introduction to the idealized structural unit method for nonlinear analysis of large plated structures and its application. Thin-Walled Struct 2003;41:329–55.